

Morphological symmetries in robotics

The journal title
XX(X):1–20
©The Author(s) 2023
Reprints and permission:
sagepub.co.uk/journalsPermissions.nav
DOI: 10.1177/ToBeAssigned
www.sagepub.com/

SAGE

Daniel Ordoñez Apraez,^{2,3} Giulio Turrisi,² Vladimir Kostic,³ Mario Martin,⁴ Antonio Agudo,⁴ Francesc Moreno-Noguer,⁴ Massimiliano Pontil,³ Claudio Semini,² and Carlos Mastalli^{1,5}

Abstract

We present a comprehensive framework for studying and leveraging morphological symmetries in robotic systems. These are intrinsic properties of the robot's morphology, frequently observed in animal biology and robotics, which stem from the replication of kinematic structures and the symmetrical distribution of mass. We illustrate how these symmetries extend to the robot's state space and both proprioceptive and exteroceptive sensor measurements, resulting in the equivariance of the robot's equations of motion and optimal control policies. Thus, we recognize morphological symmetries as a relevant and previously unexplored physics-informed geometric prior, with significant implications for both data-driven and analytical methods used in modeling, control, estimation and design in robotics. For data-driven methods, we demonstrate that morphological symmetries can enhance the sample efficiency and generalization of machine learning models through data augmentation, or by applying equivariant/invariant constraints on the model's architecture. In the context of analytical methods, we employ abstract harmonic analysis to decompose the robot's dynamics into a superposition of lower-dimensional, independent dynamics. We substantiate our claims with both synthetic and real-world experiments conducted on bipedal and quadrupedal robots. Lastly, we introduce the repository [MORPHOSYMM](#) to facilitate the practical use of the theory and applications outlined in this work.

Keywords

Symmetries, Equivariant Dynamics and Control, Geometric Learning, Invariances

1 Introduction

The field of robotics has recently witnessed a surge in the adoption of data-driven methods for modeling, estimation, and control. This trend is primarily fueled by several factors: (i) the ability of these methods to process complex data measurements, such as depth images, tactile sensing, and time-series data; (ii) their capacity to handle dynamic phenomena that are difficult to model, like friction and backlash; and (iii) their potential to bypass restrictive modeling/mathematical assumptions, such as the Markov property or ideal actuator dynamics. However, these methods often require high quantity and quality training data, which can be challenging, risky, or even impossible to obtain in robotics, especially for agile behaviors.

To mitigate this data dependency, contemporary machine learning methods aim to incorporate geometric priors, including symmetries and physics-informed inductive biases, into the learning process (Bronstein et al. 2021; Brehmer et al. 2023; Weiler et al. 2023; De Haan et al. 2023). These priors have been instrumental in the success and interpretability of traditional computational methods for modeling, estimation, and control. In this work, we characterize the morphological symmetries of robot as a type of physics-informed geometric prior. When effectively leveraged in data-driven methods, these symmetries can enhance the sample efficiency and generalization of machine learning models for modeling, estimation, and control in robotics. Thus, this approach significantly mitigates the challenges of data collection in robotics.

Essentially, morphological symmetries are structural symmetries of a robot's body that allow the robot to reconfigure itself to mimic some spatial transformations (i.e., rotations, reflections and/or translations). The simplest and most common example of such symmetries is the bilateral/sagittal symmetry in humans and many animals, where each side of the body is a mirror image of the other. This symmetry allows individuals to easily mimic a mirrored body pose by simply permuting the roles of their arms and legs. While this bilateral symmetry is common in both humans and robotic systems, robots can exhibit a broader number of such symmetries. For instance, certain quadruped robots have the ability to mimic up to eight distinct spatial transformations, as illustrated in fig. 1.

The primary incentive for studying these symmetries in practice is that they serve as a significant geometric prior when modeling and controlling the temporal evolution of the robot. This is because morphological symmetries manifest in the robot's state vector space, equations of motion, control policies, and proprioceptive and exteroceptive sensor data measurements used to perceive the robot's environment.

¹Robot Motor Intelligence – Heriot-Watt University

²Dynamic Legged Systems – Istituto Italiano di Tecnologia (IIT)

³Computational Statistics and Machine Learning – IIT

⁴Institut de Robòtica i Informàtica Industrial, CSIC-UPC

⁵IHMC Robotics – Florida Institute for Human & Machine Cognition

Corresponding author:

Daniel Felipe Ordoñez Apraez. daniel.ordonez@iit.it

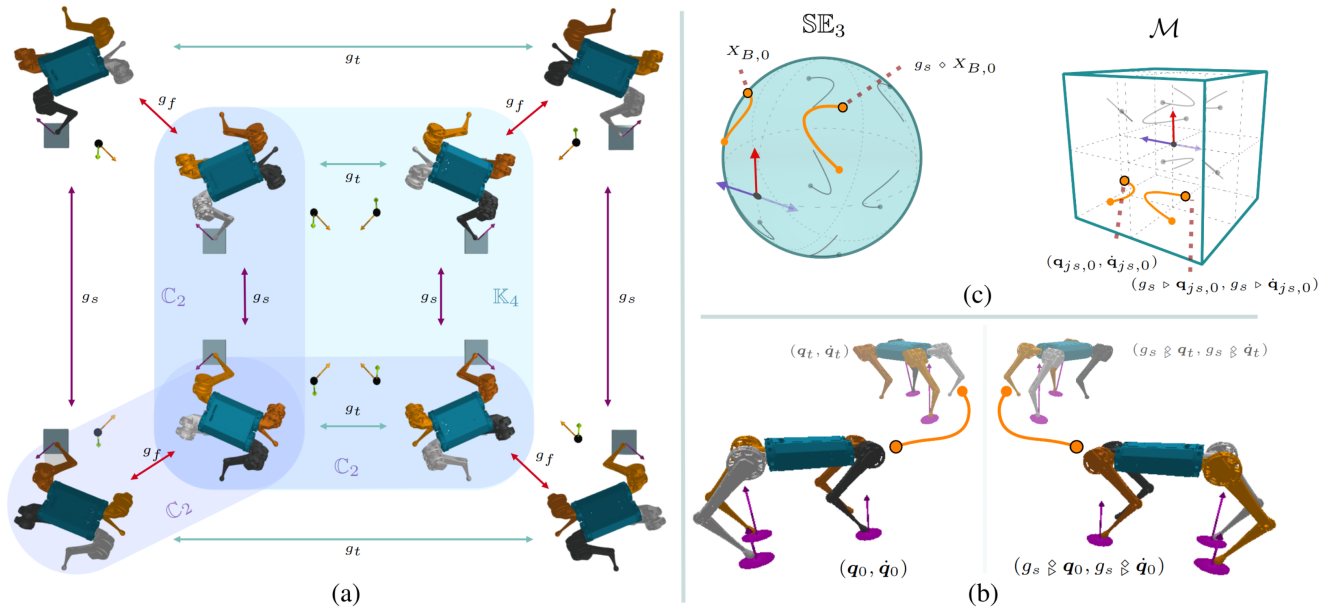


Figure 1. (a) The Mini Cheetah quadruped robot (Katz et al. 2019) exhibits a $G = C_2 \times C_2 \times C_2$ morphological symmetry, capable of mimicking three orthogonal spatial reflections g_s , g_t , and g_f , and their combinations, resulting in eight dynamically equivalent states (see [animation¹](#)). (b)-(c) These symmetries extend to the robot’s temporal evolution, control policies, and configuration space. (see [animation²](#)). The trajectories of these eight states, are depicted in the symmetric joint-space configuration space \mathcal{M} and the special Euclidean group manifold SE_3 , represent the position and orientation of the robot’s base body in space.

Intuitively, when a person encounters an obstacle with their right leg while walking, the optimal visuomotor control response, required to react and balance, is essentially a mirrored version of the reaction if the mirrored event happens with the left leg. This is because the dynamics of both mirrored body poses at the moment of contact are equivalent (up to a reflection), implying that the optimal control policy should also be symmetric and respond equivalently to these mirrored events. The same reasoning applies to the 8 equivalent states of the Mini Cheetah robot in fig. 1 (see [animation 1](#)).

Despite the significance of this geometric prior, morphological symmetries are often overlooked in both data-driven and analytical methods for modeling, control, and estimation. This is primarily because analytical models of rigid body dynamics, commonly used in robotics, implicitly leverage these symmetries due to their accurate representation of physics. Therefore, incorporating morphological symmetries into data-driven methods can be seen as a way to transfer one of the key inductive biases in analytical models to the data-driven paradigm.

Furthermore, analytical models can significantly benefit from the explicit exploitation of these symmetries. By employing abstract harmonic analysis, we show that robots with morphological symmetries possess a block-diagonal joint-space mass matrix. This structure allows us to express the robot’s dynamics as a superposition of independent lower-dimensional dynamics, as detailed in section 5.5.

Structural symmetries in physics Morphological symmetries in robotics share similarities with structural symmetries in particle physics, often referred to as point-group symmetries (Dresselhaus et al. 2007, 8.3). In physics, these symmetries arise from the replication of identical particles or atoms within molecules, atoms, or crystal structures. The principles underlying these symmetries, along with the

analytical and data-driven methods used to exploit them in both traditional and contemporary atomistic and molecular dynamics (Cornwell 1997; Noé et al. 2020; Jumper et al. 2021; Klein et al. 2023), can be transferred to robotics. However, the utilization and implications of these symmetries in robotics diverge significantly from those in physics.

Unlike physics, where the primary objective is to model dynamics, the focus in robotics is on controlling these dynamics. Moreover, the morphology of a robot is a stable and often controlled aspect of the system, unlike in physics where symmetries are subject to temporal changes with the gain or loss of particles. This stability in robotics renders these symmetries a consistent inductive bias, unaffected by time, specific motion tasks, or the operational environment. These properties, combined with the precision in the design and manufacturing of mechanical systems, and the numerical benefits associated with morphological symmetries, provide a design space of robotic systems for optimally leveraging this geometric prior.

Contributions

This work introduces a comprehensive theoretical and practical framework for studying and leveraging morphological symmetries in robotics. These structural symmetries, inherent of a robot’s body, extend to symmetries in the system’s state space and dynamics. Our aim is to formally define these symmetries, characterize their conditions of existence, and elucidate their implications in both analytical and data-driven methods. While these symmetries are readily identifiable in simple systems with basic symmetry groups, such as bilateral symmetry, our theoretical framework paves the way for identifying and exploiting morphological symmetries in complex real-world robotic systems. This includes humanoids, quadrupeds, wheeled robots, drones, modular,

soft, and continuum robots. Our contributions, which can be summarized as follows, involve:

- ❖ Characterizing how morphological symmetries manifest as symmetries in the system’s state space, sensor readings, and the equivariance of the equations of motion and optimal control policies.
- ❖ Identifying the generalized mass matrix’s equivariance as the defining property of symmetric robotic systems.

In the context of rigid body dynamics, this enable us to:

- * Establish the conditions for morphological symmetry existence, defined as analytical constraints on the robot’s kinematic and dynamic parameters (sections 5.2 and 5.3). Using these, we introduce an algorithm for the systematic identification of these symmetries (section 5.4).
- * Employ abstract harmonic analysis to leverage the symmetric structure in the robot’s joint-space (section 5.5). This approach enables us to decompose the joint-space dynamics into a superposition of lower-dimensional, independent, and simpler dynamics.

To promote the use of the theory and tools developed in this work, we present the repository [MORPHOSYMM](#),³ which facilitates the use of data augmentation, dynamics harmonics analysis, and the construction of equivariant/invariant neural networks, using [ESCNN](#) (Cesa et al. 2021), for a growing [library](#) of symmetric robots.

This paper extends our previous work (Ordóñez-Apraéz et al. 2023), by providing a more comprehensive analysis of morphological symmetries, an extended study on the conditions for their existence in rigid body dynamics, and by introducing the use of abstract harmonic analysis to leverage the symmetric structure of the robot’s joint-space dynamics.

Outline

We begin by introducing group and representation theory from a robotics perspective in section 2, followed by a discussion on symmetries in Lagrangian mechanics in section 3. The concept of morphological symmetries is presented in section 4, while section 5 delves into their application in rigid body dynamics, including the conditions for symmetry existence and the identification of the symmetry group. We also introduce the use of harmonic analysis on the system’s joint space. Section 6 provides an overview of morphological symmetries applications, such as data augmentation, equivariant/invariant function approximation, and dynamics harmonics analysis. Finally, section 7 presents our experiments and results, with concluding remarks given in section 8.

2 Background

Here, we provide an introduction to group and representation theory, the mathematical frameworks essential for studying symmetries. We aim to familiarize readers with the key concepts and notation that will be used throughout this article. As these fields might be unfamiliar in the context of robotics, we suggest an initial read-through for a general understanding, and revisiting each concept as they are referenced in the following sections. For a more

comprehensive introduction, we recommend the works of Weiler et al. (2023) for a machine learning perspective, and Selig (2005); Lanczos (2020) for insights into robotics.

2.1 Symmetry Groups

In essence, a symmetry of an object, whether it be a vector space, a manifold, or a robot, refers to an invertible transformation that preserves a significant property of the object, such as the vector space metric, the curvature of the manifold, or the energy of the robot.

Group theory studies sets of symmetry transformations as abstract mathematical constructs independent of the objects with which these symmetries are associated. This abstraction proves beneficial in our work, as it facilitates the analysis of the symmetries inherent in the laws of physics, various robotic systems, and sensor data measurements, all as distinct manifestations of the same symmetry group.

A symmetry group is a set of invertible symmetry transformations, denoted as $\mathbb{G} = \{e, g_1, g_1^{-1}, g_2, \dots\}$. This set is closed under the operations of *composition* $\circ: \mathbb{G} \times \mathbb{G} \rightarrow \mathbb{G}$, and *inversion* $(\cdot)^{-1}: \mathbb{G} \rightarrow \mathbb{G}$. This implies that for any $g_1, g_2 \in \mathbb{G}$, the composition $g_1 \circ g_2$ is also a member of \mathbb{G} . Similarly, for any $g \in \mathbb{G}$, the inverse g^{-1} belongs to \mathbb{G} and satisfies $g^{-1} \circ g = e$, where e is the identity (or trivial) transformation. Groups are characterized by their structure, defined by their order $|\mathbb{G}|$, which represents the number of unique elements in the group, and the composition rules of these elements. For example, consider the simplest group, the reflection group $\mathbb{C}_2 = \{e, g_s \mid g_s^2 = e\}$, composed of the trivial transformation and a reflection transformation g_s , characterized by $g_s^2 := g_s \circ g_s = e$.

Group structure and subgroups To comprehend the structure of a symmetry group, it is often beneficial to break it down into simpler symmetry groups and analyze how these smaller groups interact to form the larger structure. For example, the symmetry group \mathbb{G} of the Mini Cheetah robot in fig. 1, is of order $|\mathbb{G}| = 8$, and can be defined as the direct product of three distinct reflection groups, $\mathbb{G} = \mathbb{C}_2 \times \mathbb{C}_2 \times \mathbb{C}_2$ as depicted in fig. 2.

A subset of a group of symmetries, $\mathbb{G}' \subset \mathbb{G}$, is a symmetry subgroup if the subset is closed under composition and inversion, which is denoted as $\mathbb{G}' < \mathbb{G}$. In our example above, the group \mathbb{G} contains three distinct subgroups of two elements each: $\{e, g_s\}$, $\{e, g_t\}$, and $\{e, g_f\}$, depicted in fig. 2.

Although these three reflections describe distinct transformations, these groups are structurally equivalent or *isomorphic* (iso~“same” and morphic~“shape/structure”) to a reflection group. This means that, there exists a bijective map between the elements of the two groups, and this map preserves the group’s structure. We denote the isomorphism property as $\{e, g_s\} \cong \{e, g_t\} \cong \{e, g_f\} \cong \mathbb{C}_2$.

Group actions We are mostly interested in the action of a symmetry transformation on specific objects, such as the robot’s state and sensor data measurements. Therefore, we

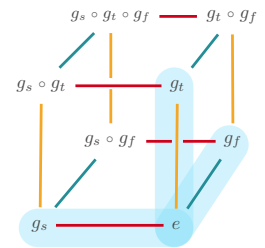


Figure 2. Structure of the group $\mathbb{G} = \mathbb{C}_2 \times \mathbb{C}_2 \times \mathbb{C}_2$

need to define how specific objects are transformed by an element $g \in \mathbb{G}$. Formally, the action of a symmetry transformation $g \in \mathbb{G}$ on a set \mathbb{S} is defined as a map $\triangleright: \mathbb{G} \times \mathbb{S} \rightarrow \mathbb{S}$, taking an element of the group and set and returning another set element, i.e., $g \triangleright s \in \mathbb{S}$ if $s \in \mathbb{S}$. This map is *associative* under group composition, $(g_1 \circ g_2) \triangleright s = g_1 \triangleright (g_2 \triangleright s)$, and respects the identity transformation $e \triangleright s = s$.

Group representations

To define a symmetry transformation not on a set but on a vector space $\mathcal{X} \in \mathbb{R}^n$, we utilize a *group representation*. By definition, a group representation on the space \mathcal{X} is a map $\rho_{\mathcal{X}}: \mathbb{G} \rightarrow \mathbb{GL}(\mathcal{X})$ that assigns invertible matrices (or linear maps) to group elements. This allows us to model the group composition operator as matrix-matrix multiplication, i.e., $\rho_{\mathcal{X}}(g_1 \circ g_2) = \rho_{\mathcal{X}}(g_1)\rho_{\mathcal{X}}(g_2)$, symmetry inversion by matrix inversion, $\rho_{\mathcal{X}}(g^{-1}) = \rho_{\mathcal{X}}(g)^{-1}$, and the action of a symmetry on a point $\mathbf{x} \in \mathcal{X}$ to be expressed as a matrix-vector multiplication, i.e., $g \triangleright \mathbf{x} := \rho_{\mathcal{X}}(g)\mathbf{x} \in \mathcal{X}$. Note that $\mathbb{GL}(\mathcal{X})$ is the group of invertible linear maps on \mathcal{X} . Whenever a vector space possesses a group representation, we refer to it as a *symmetric space*.

\mathbb{G} -invariant and \mathbb{G} -equivariant maps A map between two symmetric vector spaces $f: \mathcal{X} \rightarrow \mathcal{Y}$ often falls within two categories: group invariant or group equivariant. The map f is considered \mathbb{G} -invariant if its output remains unchanged regardless of the transformation applied to the input. Instead, a map is considered \mathbb{G} -equivariant when the result of applying a transformation to the input, followed by computing the function, is equivalent to first computing the function and then applying the transformation to the output. Formally, these conditions can be expressed as follows:

$$\underbrace{\mathbf{y} = f(\rho_{\mathcal{X}}(g)\mathbf{x})}_{\mathbb{G}\text{-invariant}} \quad \text{and} \quad \underbrace{\rho_{\mathcal{Y}}(g)\mathbf{y} = f(\rho_{\mathcal{X}}(g)\mathbf{x})}_{\mathbb{G}\text{-equivariant}} \quad | \quad \forall g \in \mathbb{G}, \mathbf{x} \in \mathcal{X}. \quad (1)$$

Symmetries as change of basis and the conjugate action The linear map $\rho_{\mathcal{X}}(g)$ can be viewed as a point transformation, mapping each point $\mathbf{x} \in \mathcal{X}$ to its symmetric counterpart $g \triangleright \mathbf{x}$, or as a change of basis in \mathcal{X} . Specifically, if $\mathbb{S}_{\mathcal{X}} = \{\bar{\mathbf{x}}_0, \dots, \bar{\mathbf{x}}_n\}$ is a basis set for the vector space, the action of g on the basis set yields another valid basis set $g \triangleright \mathbb{S}_{\mathcal{X}} := \{g \triangleright \bar{\mathbf{x}}_0, \dots, g \triangleright \bar{\mathbf{x}}_n\}$.

The action of a group element on a linear map (or matrix), which redefines the map in the symmetry-transformed basis, is referred to as the *conjugate action*. Let $\mathbf{A}: \mathcal{X} \rightarrow \mathcal{X}$ be a linear map on the symmetric vector space \mathcal{X} . The map's matrix representation depend on the chosen basis for \mathcal{X} . Therefore, under a change of basis by a given g , the map's matrix representation is redefined in the new basis as:

$$g \diamond \mathbf{A} = \rho_{\mathcal{X}}(g)\mathbf{A}\rho_{\mathcal{X}}(g)^{-1}. \quad (2)$$

The group of rigid transformations in Euclidean space In robotics theory, a fundamental group of symmetries is the group of Euclidean isometries (or rigid transformations) in d -dimensions, known as the matrix Euclidean group \mathbb{E}_d (in practise d most frequently refers to 3-dimensional space, although some toy examples will rely on $d = 2$). To define a morphological symmetry, we study this group in its abstract (non-matrix) form. Specifically, let $\mathbb{G}_E \cong \mathbb{E}_d$ denote a group

isomorphic to \mathbb{E}_d , where transformations are abstracted from their usual d -dimensional space of action. Throughout this work, we define distinct representations for these symmetry transformations. However, when we use these symmetries as transformations of points, vectors, and spatial vectors in $d + 1$ -dimensions, we default to the standard homogenous matrix representation:

$$\begin{aligned} \rho_{\mathbb{R}^{d+1}}(g) &:= \mathbf{X}_g = \begin{bmatrix} \mathbf{R}_g & \mathbf{r}_g \\ \mathbf{0} & 1 \end{bmatrix} \in \mathbb{E}_d, \\ \rho_{\mathbb{R}^d}(g) &:= \mathbf{R}_g \in \mathbb{O}_d \quad | \quad \forall g \in \mathbb{G}_E, \end{aligned} \quad (3)$$

where $\rho_{\mathbb{R}^{d+1}}$ assigns an homogeneous transformation matrix $\mathbf{X}_g \in \mathbb{E}_d$ to each $g \in \mathbb{G}_E$, representing each symmetry as an Euclidean isometry. This isometry is comprised of a rotation/reflection matrix \mathbf{R}_g , a member of the orthogonal group \mathbb{O}_d , and a translation vector $\mathbf{r}_g \in \mathbb{R}^d$. The representation $\rho_{\mathbb{R}^d}$, defaults to assigning the rotation/reflection matrix \mathbf{R}_g to each $g \in \mathbb{G}_E$. When discussing rotation, reflection, or translation actions in d -dimensions, we typically use standard robotics notation \mathbf{X}_g and \mathbf{R}_g instead of $\rho_{\mathbb{R}^{d+1}}(g)$ and $\rho_{\mathbb{R}^d}(g)$, respectively.

Inequivalent representations of Euclidean isometries The motivation behind the distinction between \mathbb{G}_E and the Euclidean group \mathbb{E}_d , is to establish distinct, inequivalent representations of Euclidean isometries. In other words, to define alternative ways for applying rotations, reflections, and translations to the robot's state. Specifically, as detailed in sections 4 and 5, we define a morphological symmetry by representing each $g \in \mathbb{G}_E$ as a transformation of the robot's joint-space configuration.

In this context, two representations of the same group, defined on the same space $\rho_{\mathcal{X}}^a, \rho_{\mathcal{X}}^b: \mathbb{G} \rightarrow \mathbb{GL}(\mathcal{X})$, are considered equivalent, denoted as $\rho_{\mathcal{X}}^a(g) \sim \rho_{\mathcal{X}}^b(g)$, if they can be related by a change of basis in \mathcal{X} . That is, if there exist a linear map $\mathbf{T}: \mathcal{X} \rightarrow \mathcal{X}$, such that:

$$\rho_{\mathcal{X}}^a(g) \sim \rho_{\mathcal{X}}^b(g) \quad \text{if} \quad \rho_{\mathcal{X}}^a(g) = \mathbf{T}\rho_{\mathcal{X}}^b(g)\mathbf{T}^{-1} \quad | \quad \forall g \in \mathbb{G}. \quad (4)$$

Decomposition of group representations Given two group representations, $\rho_{\mathcal{X}}$ and $\rho_{\mathcal{Y}}$, acting on distinct vector spaces \mathcal{X} and \mathcal{Y} respectively, we can construct a new group representation on the space $\mathcal{X} \times \mathcal{Y}$. This construction, known as the direct sum, effectively combines the two representations into a block-diagonal form. Formally, the direct sum of two representations is defined as follows:

$$\rho_{\mathcal{X} \times \mathcal{Y}}(g) = \rho_{\mathcal{X}}(g) \oplus \rho_{\mathcal{Y}}(g) := \begin{bmatrix} \rho_{\mathcal{X}}(g) & \mathbf{0} \\ \mathbf{0} & \rho_{\mathcal{Y}}(g) \end{bmatrix} \quad | \quad \forall g \in \mathbb{G}. \quad (5)$$

In sections 6 and 7, we utilize the direct sum to build group representations on spaces derived from different sensor data measurements. Conversely, in section 5.5, we decompose the representation acting on the robot's joint-space into a block-diagonal form. This decomposition, known as an *isotypic decomposition*, is a key result from abstract harmonic analysis. We introduce it here to facilitate the study of symmetries inherent in the robot's morphology.

The isotypic decomposition and isotypic basis Let $\rho_{\mathcal{X}}$ be a group representation on the finite dimensional vector space \mathcal{X} . The isotypic decomposition is the process of decomposing \mathcal{X} into an orthogonal sum of *isotypic subspaces* (iso~"same" and typic~"type of symmetries"). Each of these subspaces is invariant under the action of the

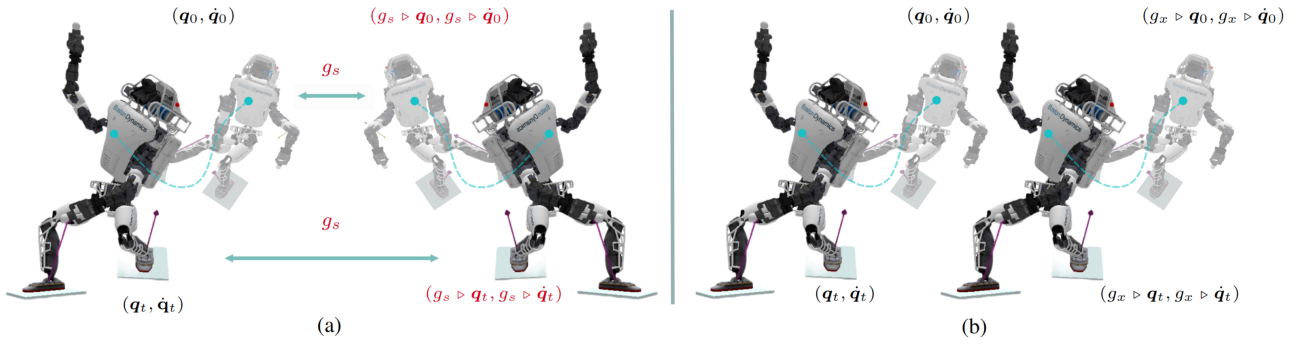


Figure 3. (a) The temporal evolution of the robot Boston Dynamics’ Atlas robot, when subjected to a horizontal spatial reflection, results in an unreachable state $(g_s \triangleright \mathbf{q}, g_s \triangleright \dot{\mathbf{q}})$, consequence of the physical inability to apply reflections to rigid bodies (Selig 2005, 2.5). Despite this, the dynamics of the original state $(\mathbf{q}, \dot{\mathbf{q}})$ and its virtual counterpart are equivalent up to a reflection of space, maintaining their temporal evolution related by the symmetry g_s . (b) Similarly, the temporal evolution of the original state and a horizontally translated state $(g_x \triangleright \mathbf{q}, g_x \triangleright \dot{\mathbf{q}})$ remain equivariant, with g_x being a feasible symmetry transformation.

group \mathbb{G} . Therefore, the isotypic decomposition is analog to the decomposition of the group representation into the direct sum of the representations $\rho_{\mathcal{X}_k}$ acting on each isotypic subspace \mathcal{X}_k .

$$\begin{aligned} \mathcal{X} &= \mathcal{X}_1 \oplus^\perp \mathcal{X}_2 \oplus^\perp \dots \oplus^\perp \mathcal{X}_{n_{iso}} = \bigoplus_{k=1}^{\perp n_{iso}} \mathcal{X}_k, \\ \rho_{\mathcal{X}} &\sim \rho_{\mathcal{X}_1} \oplus \rho_{\mathcal{X}_2} \oplus \dots \oplus \rho_{\mathcal{X}_{n_{iso}}} = \bigoplus_{k=1}^{\perp n_{iso}} \rho_{\mathcal{X}_k}. \end{aligned} \quad (6)$$

Shur’s lemma (Knapp 1986, Prop 1.5), which asserts the orthogonality of isotypic components, is a key result that we exploit in section 5.5. This orthogonality property allows us to decompose the dynamics in the robot’s joint-space into independent subspaces, each corresponding to an isotypic component. For details on the isotypic decomposition, refer to Golubitsky et al. (2012, Thm-2.5).

3 Symmetries in Lagrangian mechanics

In the context of dynamical systems, a symmetry is interpreted as a transformation that associates distinct system states with identical or equivalent dynamics. Essentially, this means that if two states are connected by a symmetry transformation, the temporal evolution of one state mirrors the symmetry-transformed temporal evolution of the other (see fig. 3a and animation 2).

To formalize this property in robotics, we shall study symmetries from the lens of Lagrangian mechanics, a modeling framework applicable to a wide range of robot types, including rigid body, continuum, soft, and modular robots. To that end, we measure the robot’s state through generalized position coordinates $\mathbf{q} \in \mathcal{Q} \subseteq \mathbb{R}^{n_q}$ and velocity coordinates $\dot{\mathbf{q}} \in \mathcal{T}_q \mathcal{Q} \subseteq \mathbb{R}^{n_q}$, where \mathcal{Q} denotes the constrained configuration space (a smooth manifold), and $\mathcal{T}_q \mathcal{Q}$ represents the configuration tangent space at \mathbf{q} (a local tangent plane). Thus, the system’s state is numerically represented as a point in the *phase space* $(\mathbf{q}, \dot{\mathbf{q}}) \in \mathcal{Q} \times \mathcal{T}_q \mathcal{Q} \subseteq \mathbb{R}^{2n_q}$. The system’s dynamics, i.e., the temporal evolution of points in the phase space, are governed by the system’s equations of motion (EoM). These are derived from the Euler-Lagrange differential equations, according to the principle of least action (Lanczos 2020, II.11):

$$\frac{d}{dt} \frac{\partial L(\mathbf{q}, \dot{\mathbf{q}})}{\partial \dot{\mathbf{q}}} - \frac{\partial L(\mathbf{q}, \dot{\mathbf{q}})}{\partial \mathbf{q}} = \mathbf{0} \iff \underbrace{M(\mathbf{q})\ddot{\mathbf{q}}}_{\text{inertial}} = \underbrace{\tau(\mathbf{q}, \dot{\mathbf{q}})}_{\text{moving}} \quad (7)$$

which, in their general form, can be stated as an equivalence between inertial and moving forces in the space of generalized coordinates. In this space, $M : \mathcal{Q} \rightarrow \mathbb{R}^{n_q \times n_q}$ represents the generalized mass matrix function, and $\tau : \mathcal{Q} \times \mathcal{T}_q \mathcal{Q} \rightarrow \mathbb{R}^{n_q}$ denotes the generalized force field function, determining the effective force result of control actions, contacts, internal constraints such as joint limits, gravitational forces, and external disturbances. These EoM are entirely derived from the Lagrangian scalar function $L(\mathbf{q}, \dot{\mathbf{q}}) := T(\mathbf{q}, \dot{\mathbf{q}}) - U(\mathbf{q}, \dot{\mathbf{q}})$, which measures the excess of kinetic energy T over the energy associated with mechanical work function U (Lanczos 2020).⁴

In this context, a symmetry g of a robotic system is defined as an *energy preserving* transformation relating equivalent states in distinct regions of the phase space (Wieber 2006). This property is formalized as the *invariance* of the system’s Lagrangian under the symmetry transformation, formally expressed as:

Definition 1. (Symmetric robotic system). *Consider a robot with generalized position coordinates $\mathbf{q} \in \mathcal{Q} \subseteq \mathbb{R}^{n_q}$, velocity coordinates $\dot{\mathbf{q}} \in \mathcal{T}_q \mathcal{Q} \subseteq \mathbb{R}^{n_q}$, and Lagrangian $L : \mathbb{R}^{n_q} \times \mathbb{R}^{n_q} \rightarrow \mathbb{R}$. The system is deemed to possess a symmetry group \mathbb{G} if its Lagrangian is a \mathbb{G} -invariant function. That is, for every state $(\mathbf{q}, \dot{\mathbf{q}}) \in \mathcal{Q} \times \mathcal{T}_q \mathcal{Q}$, the Lagrangian remains invariant:*

$$L(\mathbf{q}, \dot{\mathbf{q}}) = L(g \triangleright \mathbf{q}, g \triangleright \dot{\mathbf{q}}) \quad | \forall g \in \mathbb{G}. \quad (8)$$

\mathbb{G} -equivariant equations of motion From a practical perspective, the importance of studying symmetry stems from the fact that these transformations link the dynamics of a state $(\mathbf{q}, \dot{\mathbf{q}})$ with that of the symmetry-transformed state $(g \triangleright \mathbf{q}, g \triangleright \dot{\mathbf{q}})$. This suggests that modeling and controlling our robotic system in the vicinity of a state suffices to model and control the robot in the vicinity of *all* symmetric states.

This property is characterized by the \mathbb{G} -equivariance of the system’s EoM (Wheeler 2014), obtained from deriving the EoM in the original and symmetry transformed coordinates, as displayed in eq. (9).

The \mathbb{G} -invariant Lagrangian and the \mathbb{G} -equivariant EoM are equivalent statements that define the conditions under which a symmetry exists. Specifically, eq. (9) defines a symmetry as a transformation that relates the instantaneous inertial and moving forces impacting symmetric states.

$$\begin{aligned}
\frac{d}{dt} \frac{\partial L(\mathbf{q}, \dot{\mathbf{q}})}{\partial \dot{\mathbf{q}}} - \frac{\partial L(\mathbf{q}, \dot{\mathbf{q}})}{\partial \mathbf{q}} &= \mathbf{0} = \frac{d}{dt} \frac{\partial L(g \triangleright \mathbf{q}, g \triangleright \dot{\mathbf{q}})}{\partial (g \triangleright \dot{\mathbf{q}})} - \frac{\partial L(g \triangleright \mathbf{q}, g \triangleright \dot{\mathbf{q}})}{\partial (g \triangleright \mathbf{q})} \\
\frac{d}{dt} \frac{\partial L(\mathbf{q}, \dot{\mathbf{q}})}{\partial \dot{\mathbf{q}}} - \frac{\partial L(\mathbf{q}, \dot{\mathbf{q}})}{\partial \mathbf{q}} &= \mathbf{0} = \left[\frac{d}{dt} \frac{\partial L(g \triangleright \mathbf{q}, g \triangleright \dot{\mathbf{q}})}{\partial \dot{\mathbf{q}}} \right] \frac{\partial \dot{\mathbf{q}}}{\partial (g \triangleright \dot{\mathbf{q}})} - \left[\frac{\partial L(g \triangleright \mathbf{q}, g \triangleright \dot{\mathbf{q}})}{\partial \mathbf{q}} \right] \frac{\partial \mathbf{q}}{\partial (g \triangleright \mathbf{q})} \\
\frac{d}{dt} \frac{\partial L(\mathbf{q}, \dot{\mathbf{q}})}{\partial \dot{\mathbf{q}}} - \frac{\partial L(\mathbf{q}, \dot{\mathbf{q}})}{\partial \mathbf{q}} &= \mathbf{0} = \left[\frac{d}{dt} \frac{\partial L(g \triangleright \mathbf{q}, g \triangleright \dot{\mathbf{q}})}{\partial \dot{\mathbf{q}}} - \frac{\partial L(g \triangleright \mathbf{q}, g \triangleright \dot{\mathbf{q}})}{\partial \mathbf{q}} \right] \rho_{\mathcal{Q}}(g)^{-1} \\
g \triangleright [M(\mathbf{q})\ddot{\mathbf{q}} - \tau(\mathbf{q}, \dot{\mathbf{q}})] &= \mathbf{0} = M(g \triangleright \mathbf{q})g \triangleright \ddot{\mathbf{q}} - \tau(g \triangleright \mathbf{q}, g \triangleright \dot{\mathbf{q}}) = \mathbf{0}
\end{aligned} \tag{9}$$

This property provides a pathway for characterizing and identifying properties of symmetric systems.

Proposition 1. (Symmetric robots exhibit \mathbb{G} -equivariant mass matrix and control policies). *Reframing eq. (9) as an equality constraint of inertial and moving forces between symmetric states, we deduce that for a symmetry to exist, both the generalized mass matrix M and force field τ need to be \mathbb{G} -equivariant, i.e.,*

$$\begin{aligned}
g \diamond M(\mathbf{q}) &= M(g \triangleright \mathbf{q}), \quad \text{and} \\
g \triangleright \tau(\mathbf{q}, \dot{\mathbf{q}}) &= \tau(g \triangleright \mathbf{q}, g \triangleright \dot{\mathbf{q}}).
\end{aligned} \tag{10}$$

The equivariance of M implies that the inertial properties at the configuration $g \triangleright \mathbf{q}$ are equivalent (up to a symmetry-induced change of basis) to those of the configuration \mathbf{q} (refer to eq. (2)). Similarly, the equivariance of the τ requires that both the system's passive dynamics and control policy are \mathbb{G} -equivariant functions. As discussed in section 6.2, optimal control policies for symmetric robotic systems are inherently equivariant.

To build an intuitive understanding, consider the Atlas robot shown in fig. 3a. Here, the symmetry g_s , representing a reflection of space, relates two symmetric system states $(\mathbf{q}_0, \dot{\mathbf{q}}_0)$ and $(g_s \triangleright \mathbf{q}_0, g_s \triangleright \dot{\mathbf{q}}_0)$. As per eq. (8), this symmetry arises from their shared kinetic and potential energies, as well as the equal work done by instantaneous contact forces. Consequently, by eq. (9), the instantaneous dynamics of both states are linked by the symmetry transformation. This means that the system's motion trajectory originating from $(\mathbf{q}_0, \dot{\mathbf{q}}_0)$ will mirror the motion trajectory starting from $(g_s \triangleright \mathbf{q}_0, g_s \triangleright \dot{\mathbf{q}}_0)$, after applying the transformation g_s . Moreover, by eq. (10), the symmetric relationship between the motion trajectories is maintained as long as the forces acting on both systems, including contacts and control actions, remain related by the symmetry transformation. A similar analysis holds when considering the translation symmetry group $\mathbb{G} = \mathbb{T}_x$ for the Atlas robot (fig. 3b), where each $g \in \mathbb{T}_x$ represents a horizontal translation of the robot and the environment.

Feasible and unfeasible symmetries In our analysis, we distinguish between *feasible* symmetries, which yield another reachable state within the constrained phase space $(g \triangleright \mathbf{q}, g \triangleright \dot{\mathbf{q}}) \in \mathcal{Q} \times \mathcal{T}_{g \triangleright \mathbf{q}} \mathcal{Q}$, for any given state $(\mathbf{q}, \dot{\mathbf{q}})$ (e.g., $g \in \mathbb{T}_x$ in fig. 3b), and *unfeasible* symmetries, which lead to states outside of the constrained phase space. Infeasible symmetries can occur when g involves a reflection of bodies (see fig. 3a), or when the resultant state violates some state constraint.

Floating base robotic systems In our study of locomoting and fixed-base robotic systems, we assume, without loss of generality, that our robot is a floating-base dynamical system evolving in \mathbb{R}^d . The system's configuration is decoupled into $\mathbf{q} = (\mathbf{X}_B, \mathbf{q}_{js})$, and the system's velocity coordinates into $\dot{\mathbf{q}} = (\dot{\mathbf{X}}_B, \dot{\mathbf{q}}_{js})$. Here, $\mathbf{X}_B := \begin{bmatrix} R_B^B & \mathbf{r}_B \\ \mathbf{0} & \mathbf{1} \end{bmatrix} \in \mathbb{SE}_d$ defines

the base's position $\mathbf{r}_B \in \mathbb{R}^d$ and orientation $\mathbf{R}_B \in \mathbb{SO}_d$, and $\dot{\mathbf{X}}_B := \begin{bmatrix} [\mathbf{w}_B]_{\times} & \dot{\mathbf{r}}_B \\ \mathbf{0} & \mathbf{0} \end{bmatrix} \in \mathfrak{se}_d$ is the element of the \mathbb{SE}_d Lie algebra characterizing the base's linear $\dot{\mathbf{r}}_B \in \mathbb{R}^d$ and angular velocity $\mathbf{w}_B \in \mathbb{R}^d$, parameterized in skew symmetric matrix form $[\mathbf{w}_B]_{\times} \in \mathfrak{so}_d$, as an element of the \mathbb{SO}_d Lie algebra (Solà et al. 2021). Similarly, $\mathbf{q}_{js} \in \mathcal{M} \subseteq \mathbb{R}^{n_j}$ and $\dot{\mathbf{q}}_{js} \in \mathcal{T}_q \mathcal{M} \subseteq \mathbb{R}^{n_j}$ describe the joint space configuration and velocity coordinates of the robot's n_j internal degrees of freedom (DoF) (Ostrowski and Burdick 1996).

4 Morphological Symmetries

Morphological symmetries are intuitively associated with the ability of certain robotic systems to emulate Euclidean isometries—such as spatial rotations, reflections, or translations—through feasible state transformations. This means that the robot can assume multiple state configurations, each yielding a state equivalent to the one transformed by the isometry under the system's dynamics. A defining feature of these symmetries is that they are inherent properties of the robot, unaffected by time, specific motion tasks, or the operating environment. They stem from morphological or structural similarities, resulting from replicated kinematic chains and body parts with symmetric mass distributions.

Before a formal definition, let us consider the Atlas humanoid robot, which possesses the simplest morphological symmetry group, the reflection group $\mathbb{G} = \mathbb{C}_2$. In fig. 4a, the robot undergoes an unfeasible symmetry transformation (involving the physically unrealizable reflection of rigid bodies), leading to the unreachable state $(g_s \triangleright \mathbf{q}, g_s \triangleright \dot{\mathbf{q}})$. Conversely, in fig. 4b, the robot experiences a feasible state transformation, resulting in the equivalent state $(g_s \otimes \mathbf{q}, g_s \otimes \dot{\mathbf{q}})$. This transformation implies that the reflectional symmetry g_s has two inequivalent representations (refer to section 6.2) describing different transformations of the robot's state, that are defined as:

$$\begin{aligned}
(g_s \triangleright \mathbf{q}, g_s \triangleright \dot{\mathbf{q}}) &:= \left(\begin{bmatrix} \mathbf{X}_{g_s} \mathbf{X}_B \\ \mathbf{q}_{js} \end{bmatrix}, \begin{bmatrix} \mathbf{X}_{g_s} \dot{\mathbf{X}}_B \\ \dot{\mathbf{q}}_{js} \end{bmatrix} \right) \quad \text{and} \\
(g_s \otimes \mathbf{q}, g_s \otimes \dot{\mathbf{q}}) &:= \left(\begin{bmatrix} \mathbf{X}_{g_s} \mathbf{X}_B \mathbf{X}_{g_s}^{-1} \\ \rho_{\mathcal{M}}(g_s) \mathbf{q}_{js} \end{bmatrix}, \begin{bmatrix} \mathbf{X}_{g_s} \dot{\mathbf{X}}_B \mathbf{X}_{g_s}^{-1} \\ \rho_{\mathcal{T}_q \mathcal{M}}(g_s) \dot{\mathbf{q}}_{js} \end{bmatrix} \right).
\end{aligned} \tag{11}$$

The transformation $g_s \triangleright \mathbf{q}$ involves a reflection of the robot's bodies without altering the joint space configuration. In contrast, the feasible transformation $g_s \otimes \mathbf{q}$ entails a reorientation of the base's body $g \diamond \mathbf{X}_B := \mathbf{X}_{g_s} \mathbf{X}_B \mathbf{X}_{g_s}^{-1} \in \mathbb{SE}_d$ (refer to eq. (2)), along with a non-trivial transformation of the joint-space (or internal) configuration $g \triangleright \mathbf{q}_{js} := \rho_{\mathcal{M}}(g_s) \mathbf{q}_{js}$. We will denote this action by the operator \otimes .

A similar analysis applies to the Mini Cheetah quadruped robot, which possesses a larger morphological symmetry group of order $|\mathbb{G}| = 8$ (see fig. 1). Focusing on the subgroup $\{e, g_r\} < \mathbb{G}$, in fig. 4c, the robot and its environment undergo a feasible symmetry representing a 180° rotation, resulting in the reachable state $(g_r \triangleright \mathbf{q}, g_r \triangleright \dot{\mathbf{q}})$. Moreover, on

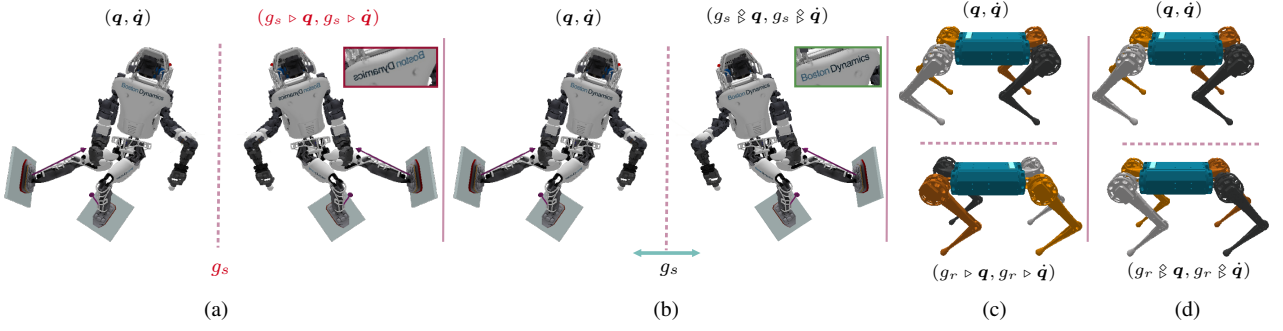


Figure 4. (a) Atlas robot undergoing an unfeasible horizontal spatial reflection g_s , leading to an unreachable state $(g_s \triangleright \mathbf{q}, g_s \triangleright \dot{\mathbf{q}})$. (b) The same robot experiencing a feasible horizontal spatial reflection g_s through a morphological symmetry, resulting in a reachable equivalent state $(g_s \boxtimes \mathbf{q}, g_s \boxtimes \dot{\mathbf{q}})$. (c) Mini Cheetah robot subjected to a feasible 180° rotation g_r , yielding the equivalent state $(g_r \triangleright \mathbf{q}, g_r \triangleright \dot{\mathbf{q}})$. (d) The same robot undergoing a feasible 180° rotation g_r through a morphological symmetry, leading to the reachable equivalent state $(g_r \boxtimes \mathbf{q}, g_r \boxtimes \dot{\mathbf{q}})$.

fig. 4d, an equivalent state $(g_r \boxtimes \mathbf{q}, g_r \boxtimes \dot{\mathbf{q}})$ is reached with a different state transformation. In both examples, a Euclidean isometry $g_r, g_s \in \mathbb{G}_E$ alters the robot and its environment, leading to a system state that may be reachable or unreachable, but is equivalent to the reachable state obtained through a different feasible state transformation. This feasible transformation is defined through a reorientation of the robot’s base body and non-trivial transformation of its joint space configuration. This critical property can be formalized for any robotic system as follows:

Definition 2. (Morphological Symmetry). *Consider a robot with generalized position coordinates $\mathbf{q} \in \mathcal{Q} \subseteq \mathbb{R}^{n_q}$, velocity coordinates $\dot{\mathbf{q}} \in \mathcal{T}_q \mathcal{Q} \subseteq \mathbb{R}^{n_q}$, and Lagrangian $L : \mathbb{R}^{n_q} \times \mathbb{R}^{n_q} \rightarrow \mathbb{R}$. An Euclidean isometry $g \in \mathbb{G}_E$ is deemed a system’s morphological symmetry if the action has two inequivalent representations yielding distinct symmetric states $(g \triangleright \mathbf{q}, g \triangleright \dot{\mathbf{q}})$ and $(g \boxtimes \mathbf{q}, g \boxtimes \dot{\mathbf{q}})$, that is:*

$$L(\mathbf{q}, \dot{\mathbf{q}}) = L(g \triangleright \mathbf{q}, g \triangleright \dot{\mathbf{q}}) = L(g \boxtimes \mathbf{q}, g \boxtimes \dot{\mathbf{q}}) \quad (12)$$

$$| \forall (\mathbf{q}, \dot{\mathbf{q}}), (g \boxtimes \mathbf{q}, g \boxtimes \dot{\mathbf{q}}) \in \mathcal{Q} \times \mathcal{T}\mathcal{Q}.$$

Hereafter, we denote the morphological symmetry group of a robotic system as \mathbb{G} . This group comprises all Euclidean isometries that satisfy definition 2, that is $\mathbb{G} \leq \mathbb{G}_E$. In a nutshell, the action of a morphological symmetry signifies an alternative pathway for applying specific rotations, reflections, and translations to the robot’s state.

Modeling the dynamics of symmetric systems A morphological symmetry $g \in \mathbb{G}$ can be viewed as a point transformation in the robot’s configuration space, linking any reachable state $(\mathbf{q}, \dot{\mathbf{q}})$ to its set of symmetric states, featuring *equivalent dynamics*, denoted as $\mathbb{G}(\mathbf{q}, \dot{\mathbf{q}}) = \{(g \boxtimes \mathbf{q}, g \boxtimes \dot{\mathbf{q}}) \mid g \in \mathbb{G}\}$. This relationship is a crucial geometric prior when modeling the system’s dynamics, as it requires any optimal analytical or data-driven model to be \mathbb{G} -equivariant (Ordoñez-Apaez et al. 2023, Proposition 2).

Indeed, analytical models of rigid body dynamics for systems with morphological symmetries are inherently \mathbb{G} -equivariant due to their reliance on the analytical generalized mass matrix function (eq. (10)). For symmetric robots without analytical or tractable dynamics models, such as continuum, soft, or modular robots, morphological symmetries provide a valuable geometric prior, which in practice could improve the generalization of data-driven models and mitigate the challenges posed by the curse of

dimensionality (Higgins et al. 2022; Bietti et al. 2021). For more details refer to section 6.

Control policy constraints By proposition 1, a robotic system with a symmetry group \mathbb{G} is required to possess a \mathbb{G} -equivariant control policy, as non-equivariant control forces break the \mathbb{G} -equivariance of the system’s EoM (eq. (9)). This property is of special value in the case of morphological symmetries, considering that, under mild assumptions, optimal control policies of symmetric systems are inherently \mathbb{G} -equivariant functions (Zinkevich and Balch 2001), as detailed in section 6.2.

In essence, this implies that for a bipedal system such as the Atlas robot (fig. 4b), the optimal control policy is an *ambidextrous* policy. That is, the optimal action for a state $(\mathbf{q}, \dot{\mathbf{q}})$ is equivalent to the control action for the symmetry-transformed state $(g \boxtimes \mathbf{q}, g \boxtimes \dot{\mathbf{q}})$. This principle extends to systems with larger symmetry groups, such as the Mini Cheetah robot depicted in fig. 1 (see animation 1).

Morphological constraints The presence of morphological symmetries in robotic systems, such as the Atlas robot (fig. 4) and the Mini Cheetah robot (fig. 1), is closely linked to the \mathbb{G} -equivariance of the robot’s generalized mass matrix (eq. (10)). This property arises from symmetries in mass distribution and the duplication of bodies and kinematic chains, consequence of proposition 1. For example, the Atlas robot can mimic a spatial reflection due to its sagittal symmetry and duplicated limbs, while the Mini Cheetah, with its replicated legs and symmetric cuboid torso, can emulate three spatial reflections.

To understand these morphological constraints, we are required to delve into a specific type of a robot architecture. In the following section we focus on rigid body dynamics, however, note that the analysis presented can be easily adapted to continuum, soft, and modular robots.

5 Morphological symmetries in rigid body systems

In this section, our objective is to characterize the implications of morphological symmetries in rigid body systems. These systems consist of n_b interconnected rigid bodies evolving in \mathbb{E}_d . Given that symmetries are transformations that preserve energy (definition 1), we aim to discern the symmetry constraints on the kinematic and

dynamics parameters. Concretely, we analyze the conditions of \mathbb{G} -invariance of the system's kinetic energy $T(\mathbf{q}, \dot{\mathbf{q}}) = T(g \circledast \mathbf{q}, g \circledast \dot{\mathbf{q}})$.

5.1 Rigid body systems

The kinetic energy in rigid body dynamics is calculated by summing the energies of all constituent bodies in the system: $T(\dot{\mathbf{r}}, \mathbf{w}) = \frac{1}{2} \sum_k^{n_b} m_k \dot{\mathbf{r}}_k^\top \dot{\mathbf{r}}_k + \mathbf{w}_k^\top \mathbf{I}_k \mathbf{w}_k$, where $m_k \in \mathbb{R}_+$, $\mathbf{I}_k \in \mathbb{R}^{d \times d}$, $\dot{\mathbf{r}}_k \in \mathbb{R}^d$ and $\mathbf{w}_k \in \mathbb{R}^d$ represent the mass, rotational inertia at the center of mass (CoM), linear and velocity of body k , respectively. Although this quantity can also be expressed in terms of the system's generalized coordinates and generalized mass matrix $T(\mathbf{q}, \dot{\mathbf{q}}) = \frac{1}{2} \dot{\mathbf{q}}^\top \overline{M}(\mathbf{q}) \dot{\mathbf{q}}$, we exploit the decomposition of the state into its floating-base and joint space configurations $\mathbf{q} = (\mathbf{X}_B, \mathbf{q}_{j_s})$. This is done to study the invariance of the kinetic energy of the floating-base body T_B independently from that of the joint space kinetic energy $T_{\mathcal{M}}$. These quantities are expressed as:

$$\begin{aligned} T_B(\mathbf{X}_B) &= \frac{1}{2} m_B \dot{\mathbf{r}}_B^\top \dot{\mathbf{r}}_B + \mathbf{w}_B^\top \mathbf{I}_B \mathbf{w}_B \quad \text{and} \\ T_{\mathcal{M}}(\mathbf{q}_{j_s}, \dot{\mathbf{q}}_{j_s}) &= \frac{1}{2} \dot{\mathbf{q}}_{j_s}^\top \overline{M}(\mathbf{q}_{j_s}) \dot{\mathbf{q}}_{j_s}, \end{aligned} \quad (13)$$

where

$$\overline{M}(\mathbf{q}_{j_s}) := \sum_k^{n_b-1} J_{t_k}(\mathbf{q}_{j_s})^\top m_k J_{t_k}(\mathbf{q}_{j_s}) + J_{R_k}(\mathbf{q}_{j_s})^\top \mathbf{I}_k J_{R_k}(\mathbf{q}_{j_s}) \quad (14)$$

denotes the joint space generalized mass matrix, constructed from the mass, inertia, and the position and orientation Jacobians $J_{t_k} : \mathcal{Q} \rightarrow \mathbb{R}^{d \times n_j}$ and $J_{R_k} : \mathcal{Q} \rightarrow \mathbb{R}^{d \times n_j}$ of each body. These Jacobians define the state-dependent mappings from generalized velocities to the k^{th} body's linear (${}^B \dot{\mathbf{r}}_k = J_{t_k}(\mathbf{q}_{j_s}) \dot{\mathbf{q}}_{j_s}$) and angular (${}^B \mathbf{w}_k = J_{R_k}(\mathbf{q}_{j_s}) \dot{\mathbf{q}}_{j_s}$) velocity in Euclidean space, relative to the floating-base body's frame (Wieber 2006).

The computation of these Jacobians relies on the system's kinematic parameters, which detail the relative positions and orientations of links and joints, as well as the system's dynamic parameters, which include the mass and inertia of all bodies. Since the kinetic energy is dependent on these parameters, the presence of a morphological symmetry inherently imposes constraints on the kinematic and dynamic parameter space.

5.2 Constraints on the floating-base's body mass distribution

Consider the conditions under which a morphological symmetry exists for the floating-base body only. In this case, the necessary Lagrangian \mathbb{G} -invariance from eq. (12) reduces to the equality of kinetic energy between the base body transformed by a Euclidean isometry, denoted as $g \triangleright \mathbf{X}_B$, and the body transformed by morphological symmetry, represented as $g \diamond \mathbf{X}_B$. This can be expressed as:

$$T_B(g \triangleright \mathbf{X}_B) = T_B(g \diamond \mathbf{X}_B), \quad (15)$$

where the action of the Euclidean isometry represents a potential rotation or roto-reflection of the body $\mathbf{R}_g \mathbf{R}_B \in \mathbb{O}_d$, and a morphological symmetry is restricted to a rotation $\mathbf{R}_g \mathbf{R}_B \mathbf{R}_g^\top \in \mathbb{SO}_d$, due to the feasibility requirement.

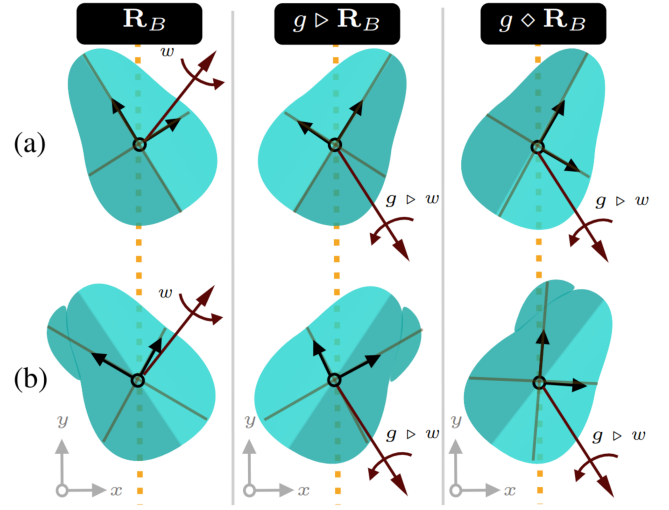


Figure 5. (a) Reflectional morphological symmetry is observed in a body with a symmetric mass distribution. For such a body, the unfeasible action of a reflection of the body, $g \triangleright \mathbf{R}_B$, results in a body configuration that mirrors the inertia and kinetic energy of the rotated body at $g \diamond \mathbf{R}_B$. (b) However, if the symmetry in mass distribution is disrupted, the states $g \triangleright \mathbf{R}_B$ and $g \diamond \mathbf{R}_B$ will exhibit different reflected inertias and kinetic energies when subjected to the equal angular velocities. This results in the body's inability to mimic a reflection of space.

Since the configurations $g \triangleright \mathbf{X}_B$ and $g \diamond \mathbf{X}_B$ generally differ, they are constrained to have the same mass distribution to ensure an equivalent dynamics. In other words, this is required to react identically to the application of a moving force (refer to fig. 5). This requirement is translated to the equality of the reflected inertia tensors:

$$\begin{aligned} (g \triangleright \mathbf{R}_B) \bar{\mathbf{I}}_B (g \triangleright \mathbf{R}_B)^{-1} &= (g \diamond \mathbf{R}_B) \bar{\mathbf{I}}_B (g \diamond \mathbf{R}_B)^{-1} \\ (\mathbf{R}_g \mathbf{R}_B) \bar{\mathbf{I}}_B (\mathbf{R}_g \mathbf{R}_B)^\top &= (\mathbf{R}_g \mathbf{R}_B \mathbf{R}_g^\top) \bar{\mathbf{I}}_B (\mathbf{R}_g \mathbf{R}_B \mathbf{R}_g^\top), \end{aligned} \quad (16)$$

where $\mathbf{I}_B = \mathbf{R}_B \bar{\mathbf{I}}_B \mathbf{R}_B^\top \in \mathbb{R}^{d \times d}$ is the reflected body inertia at the configuration \mathbf{R}_B , and $\bar{\mathbf{I}}_B$ is the body's diagonal inertia tensor in a frame aligned with the body's principal axes of inertia (Traversaro et al. 2016), which we show in fig. 5a.

The ability of a body to adopt various configurations, each sharing identical reflected inertias as defined by eq. (16), is an inherent characteristic of bodies with symmetrical mass distributions. This property introduces redundancy in the selection of orientation and handedness of a reference frame attached to the body's CoM and aligned with the body's principal axes of inertia. Consequently, this implies the existence of a group of symmetry transformations $\mathbb{G}_B \leq \mathbb{G}_E$ that can alter the body's configuration while preserving the reflected inertia tensor:

$$\mathbb{G}_B = \{g \in \mathbb{G}_E \mid \mathbf{R}_B \bar{\mathbf{I}}_B \mathbf{R}_B^\top = \mathbf{R}_B (g^{-1} \diamond \bar{\mathbf{I}}_B) \mathbf{R}_B^\top, \forall \mathbf{R}_B \in \mathbb{SO}_d\}, \quad (17)$$

in which the symmetry $g \in \mathbb{G}_B$ represents a transformation relative to the body's principal axes of inertia, i.e., $\mathbf{R}_B \mathbf{R}_g$. Fig. 5a depicts an example of the reflection along one of the bodies principal axes of inertia relating the configurations.

5.2.1 Identifying candidate morphological symmetries

The group of symmetries in the mass distribution of the robot's base \mathbb{G}_B represents the set of in-place rotations

and reflections under which the dynamics of this body remain invariant. These are interpreted as the subgroup of symmetries of Newtonian physics preserved by the floating-base's body mass distribution. Therefore, this group represents a set of potential morphological symmetries of the robot, as depicted in fig. 6a.

It is important to observe that both resulting body orientations, $g \triangleright \mathbf{R}_B = \mathbf{R}_g \mathbf{R}_B \in \mathbb{O}_n$ and $g \diamond \mathbf{R}_B = \mathbf{R}_g \mathbf{R}_B \mathbf{R}_g^T \in \mathbb{SO}_d$, share the same reflected inertias. Consequently, when subjected to identical velocities and forces, these two base configurations have equivalent dynamics, as expressed in eq. (15). Furthermore, $g \diamond \mathbf{R}_B$ represents a feasible body configuration even when g corresponds to an unfeasible isometry, such as a reflection (see fig. 5).

To understand this fact, let's consider the two bodies illustrated in fig. 5. In fig. 5a, this body exhibits a symmetric mass distribution with respect to its x principal axis of inertia, leading to $\mathbb{G}_B = \{e, g\} \simeq \mathbb{C}_2$. In contrast, in fig. 5b, this body lacks any symmetry in its mass distribution, resulting in $\mathbb{G}_B = \{e\}$. The symmetric mass distribution of body in fig. 5a enables it to emulate an otherwise unfeasible spatial reflection, $g \triangleright \mathbf{R}_B$, through a feasible rotation $g \diamond \mathbf{R}_B$. It is crucial to note that perturbing the mass distribution disrupts this reflectional symmetry, as evidenced by the differing kinetic energy of the g -transformed body and g -transformed body differ (refer to fig. 5b).

A practical example can be observed in the Mini Cheetah robot's base body depicted in fig. 1. Its cuboid body showcases three orthogonal reflectional symmetries in the Mini Cheetah's mass distribution, denoted as $\mathbb{G}_B = \{e, g_s, g_t, g_f \mid g_s^2 = g_t^2 = g_f^2 = e\}$. These symmetries result in an arbitrary selection of the reference frame attached to its body, leading to the arbitrary determination of the Mini Cheetah's forward/backward, up/down, and left/right directions.

In both instances, the group $\mathbb{G}_B \leq \mathbb{G}_E$, which describes the symmetries in the robot's base mass distribution, suggests potential Euclidean isometries that could result in morphological symmetries of the robotic system. For robotic systems with multiple unique (non-replicated) bodies (e.g., the head of the Atlas robot, see fig. 3), the group of candidate morphological symmetries is limited to the subgroup of Euclidean isometries that describe the symmetries of mass distribution of all unique bodies. Whether a candidate symmetry is indeed a morphological symmetry depends on (i) the other bodies in the system's kinematic structure and (ii) the robot's morphology admits a joint space transformation that complies with definition 2.

5.3 Constraints on the kinematic structure

Modularity in the kinematic structure, specifically the replication of identical or reflected kinematic branches (or substructures), provides the necessary conditions for the existence of joint space action transformations. In these cases, we consider Euclidean isometries $g \in \mathbb{G}_B$ as potential morphological symmetries of the robot. Concretely, given that the configuration of the floating-base body transformed by this isometry differs from the one transformed by the morphological symmetry, (i.e., $g \triangleright \mathbf{X}_B \neq g \diamond \mathbf{X}_B$ as illustrated in figs. 4 and 6), there must exist a joint space

action transformation

$$(g \triangleright \mathbf{q}_{js}, g \triangleright \dot{\mathbf{q}}_{js}) = (\rho_{\mathcal{M}}(g) \mathbf{q}_{js}, \rho_{\tau_{\mathcal{M}}}(g) \dot{\mathbf{q}}_{js}),$$

which ensures that both robot configurations exhibit equal energy states and equivalent dynamics (eq. (12)).

Modular kinematic structure Robotic systems often exhibit a balanced distribution of replicated kinematic branches within their kinematic structure. Examples include the four identical legs of the Mini Cheetah robot and the mirrored arms and legs of the Atlas robot (refer to fig. 1 and fig. 3). This replication introduces symmetries in the labeling (or ordering) of these branches, which in practice enable the interchange of role and configuration of them under the action of a morphological symmetry, to mimic the Euclidean isometry.

As an example, consider the robot in fig. 6. The symmetric mass distribution of this robot's base body, combined with its replicated limbs, results in arbitrary ordering of its three limbs. This symmetry allows the robot to replicate a 120° spatial rotation through a joint space transformation that involves a permutation of its limb configurations and ensures the equivalence of the robot's energy under the action of the morphological symmetry. Similarly, fig. 1 shows how the morphological symmetries of the Mini Cheetah robot result in the arbitrary labeling of the *front/hind* and *left/right* legs.

5.3.1 Structure of the joint space action transformation

Assume the robot has n_k unique kinematic branches, represented by the label set $\mathbb{S} = \{s_1, \dots, s_{n_k}\}$. Each branch s_i possesses $n_{dof}(s_i) \in \mathbb{N}$ DoF and is replicated $n_{rep}(s_i) \in \mathbb{N}$ times within the robot's kinematic structure. The labels for the instances of each branch s_i are denoted as $\mathbb{S}_i = \{s_{i,1}, \dots, s_{i,n_{rep}(s_i)}\}$ (see fig. 6b). As an example, consider robot Atlas, featuring as unique kinematic chains the leg, arm, and head $\mathbb{S} = \{s_{arm}, s_{leg}, s_{head}\}$. These substructures are replicated $n_{rep}(s_{arm}) = n_{rep}(s_{leg}) = 2$ and $n_{rep}(s_{head}) = 1$ times.

The action of a morphological symmetry in the joint space results in a permutation of the roles of branches with the same type, denoted as $g \triangleright s_{i,j} := s_{i,g(j)} \in \mathbb{S}_i$, where $g(j)$ is the label that j is mapped to under the permutation induced by g . This leads to the decomposition of the joint space configuration space and its associated group representation:

$$g \triangleright s_{i,j} := s_{i,g(j)} \in \mathbb{S}_i, \quad \text{and} \\ \rho_{\mathbb{S}_i}(g) \begin{bmatrix} s_{i,1} \\ s_{i,2} \\ \vdots \end{bmatrix} = \begin{bmatrix} s_{i,g(1)} \\ s_{i,g(2)} \\ \vdots \end{bmatrix} \mid \forall i \in [1, n_k], j \in [1, n_{rep}(s_i)], \quad (18)$$

where $\rho_{\mathbb{S}_i}(g)$ is the permutation representation acting on the labels of the instances of branch type s_i . Following our example with the Atlas robot, the action of g_s in fig. 4b induces a permutation of the left and right arm configurations $g \triangleright s_{arm,1} = s_{arm,2}$ and $g \triangleright s_{arm,2} = s_{arm,1}$. Given that these permutations do not mix the distinct branch types, we can adopt a basis for the joint space configuration space leading to the decomposition of its associated group representation, i.e.,

$$\mathcal{M} := \mathcal{M}_{[s_1]} \times \dots \times \mathcal{M}_{[s_{n_k}]} \subseteq \mathbb{R}^{n_j}, \quad \text{and} \\ \rho_{\mathcal{M}} := \rho_{\mathcal{M}_{[s_1]}} \oplus \dots \oplus \rho_{\mathcal{M}_{[s_{n_k}]}}. \quad (19)$$

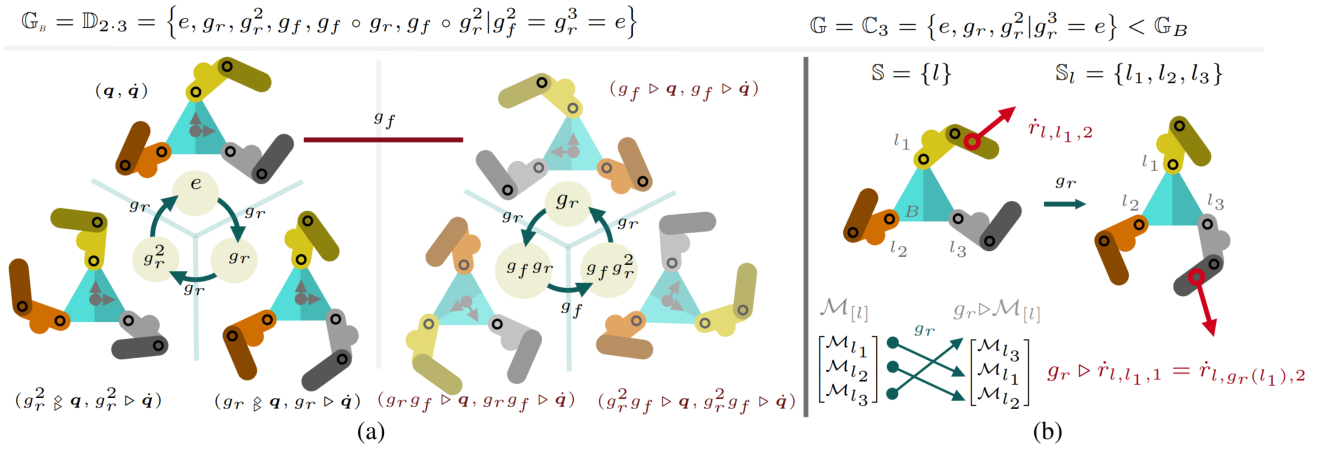


Figure 6. (a) Example robotic system, evolving in \mathbb{R}^2 , featuring a triangular base body which exhibits a symmetric mass distribution characterized by the group of 3 rotations and 3 roto-reflections, the Dihedral group $\mathbb{G}_B = \mathbb{D}_{2.3}$. However, the system's morphological symmetry is limited to the rotational subgroup, $\mathbb{G} = \mathbb{C}_3 < \mathbb{G}_B$, due to the absence of reflectional symmetry in the limbs' bodies mass distribution, which is necessary for mimicking the reflection isometry g_f with a feasible joint space transformation. (b) The base body's symmetric mass distribution results in an arbitrary labeling of the robot's limbs (l_1, l_2 and l_3), enabling the robot to mimic a 120° spatial rotation through a joint space transformation that permutes the limbs' configurations.

Each $\mathcal{M}_{[s_i]} := \bigotimes_{j=1}^{n_{rep}(s_i)} \mathcal{M}_{s_i} \subseteq \mathbb{R}^{n_{rep}(s_i)n_{dof}(s_i)}$ encapsulates the configuration space of all instances of the kinematic branch type s_i (see fig. 6b). Conversely, $\mathcal{M}_{s_i} \subseteq \mathbb{R}^{n_{dof}(s_i)}$ represents the configuration space of a single instance of type s_i . This suggests that the joint space group representation $\rho_{\mathcal{M}}$ is exclusively constructed from the n_k representations of each branch type, i.e., $[\rho_{\mathcal{M}_{s_i}}]_{i=1}^{n_k}$.

Intuitively, the transformation described by $\rho_{\mathcal{M}_{s_i}}$ implies an independent rotation/reflection of the coordinate frames attached to each joint within the kinematic branch s_i . For instance, when the branch s_i is build from 1-dimensional prismatic or revolute joints, its group representation $\rho_{\mathcal{M}_{s_i}}$ results in diagonal matrices filled with 1 and -1, describing required reflections on the axes of each DoF.

Equipped with the above-mentioned formalism, the joint space group representation is defined as:

$$\rho_{\mathcal{M}} := \begin{bmatrix} \rho_{\mathcal{M}_{[s_1]}} & & \\ & \ddots & \\ & & \rho_{\mathcal{M}_{[s_k]}} \end{bmatrix}, \quad \text{with } \rho_{\mathcal{M}_{[s_i]}} := \rho_{\mathbb{S}_i} \otimes \rho_{\mathcal{M}_{s_i}} \quad (20)$$

Where \otimes denotes the Kronecker product. This matrix product, in conjunction with the permutation of the branch's configurations $\rho_{\mathbb{S}_i}$, is responsible for ensuring that the group representation $\rho_{\mathcal{M}_{[s_i]}}$ applies the appropriate rotation/reflection of the joints coordinate frames across all branches of type s_i , as depicted in fig. 6.

5.3.2 Algebraic constraints in kinematic parameters

The approach delineated above provides insights into the internal structure of the joint space group representation, emphasizing the importance of the unique constituent group representations $\rho_{\mathcal{M}_{s_i}}$ necessary to define the group action in \mathcal{Q} . Algebraically, the validity of the action of each candidate $g \in \mathbb{G}_B$ can be verified by checking whether the transformation yields a kinematic structural symmetry—a prerequisite for the existence of a morphological symmetry. This requirement manifests as an equality between the linear velocity of each body, transformed by the group action $g \triangleright \dot{r}_{s_i, j, n}$, and the velocity of its permutation counterpart $\dot{r}_{s_i, g(j), n}$ (see fig. 6b). Here, $\dot{r}_{s_i, g(j), n}$ denotes the linear velocity of body n in the kinematic branch $s_i, g(j)$. This constraint is articulated, for any $n \in [1, n_{dof}(s_i)]$, as:

Identifying Morphological Symmetries

- 1: Identify unique bodies in the kinematic structure.
- 2: Identify the group \mathbb{G}_B of candidate MS, from the unique bodies (eq. (16)).
- 3: Identify the unique kinematic structures $\mathbb{S} = \{s_1, \dots, s_{n_k}\}$. Their configurations spaces \mathcal{M}_{s_i} , and group representations $\rho_{\mathcal{M}_{s_i}}$ (eq. (19)).
- 4: Identify the instances of the kinematic branches $\mathbb{S}_i = \{s_{i,1}, \dots, s_{i, n_{rep}(s_i)}\}$ and their associated permutations $\rho_{\mathbb{S}_i}$ (eq. (18)).
- 5: Build the group representation $\rho_{\mathcal{M}}$ (eq. (20)).
- 6: Test each $g \in \mathbb{G}_B$ following eq. (21) and eq. (13).

Figure 7. Pseudo-code for identifying the morphological symmetry group \mathbb{G} in rigid body dynamics.

$$\dot{r}_{s_i, g(j), n} = g \triangleright \dot{r}_{s_i, j, n},$$

$$J_{t_{s_i, g(j), n}}(g \triangleright \mathbf{q}_{js}) g \triangleright \dot{\mathbf{q}}_{js} = g \triangleright J_{t_{s_i, j, n}}(\mathbf{q}_{js}), \quad (21)$$

$$J_{t_{s_i, g(j), n}}(\rho_{\mathcal{M}}(g) \mathbf{q}_{js}) \rho_{\mathcal{T}_q \mathcal{M}}(g) = \mathbf{R}_g J_{t_{s_i, j, n}}(\mathbf{q}_{js}).$$

It is worth emphasizing that eq. (21) describes the constraints in the kinematic parameters of the robot's kinematic branches. An analog constraint is applied when considering the angular velocities of the bodies.

5.4 Algorithmic identification of a system's morphological symmetry group

In previous sub-sections, we outline the necessary conditions for the existence of morphological symmetry in rigid body dynamics. These include specific constraints on the robot's kinematic structure and on the mass distribution within rigid bodies. While this analysis may seem extensive for simpler systems or symmetry groups of low order, it provides a fundamental framework for studying more complex systems typically encountered in robotics. Such systems may have a larger number of DoF or symmetries, where geometric intuition alone may not be adequate. The pseudo-code in fig. 7 provides a step-by-step guide for identifying the morphological symmetry group. In the following section we motivate our theoretical analysis by demonstrating the

practical benefits of identifying the morphological symmetry group in the context of dynamic motion analysis.

5.5 Dynamics harmonics analysis

In this section, we exploit the permutation symmetries in the robot's joint-space configuration \mathcal{M} using abstract harmonic analysis. Our objective is to elucidate the numerical and modeling benefits of the *isotypic basis*, an alternative basis set for \mathcal{M} . Essentially, this basis provides an alternative coordinate frame in which the dynamics of points in \mathcal{M} are decomposed as a superposition of independent and lower-dimensional dynamics. Such decomposition leads to a finite number of subspaces, refer to as isotypic subspaces. Each subspace represents a space of symmetry-constrained robot configurations (see fig. 8).

This decomposition enables the description of any joint-space motion trajectory as a superposition of lower-dimensional symmetric and synergistic modes of motions, each governed by its own independent dynamics. We will refer to these directions of motion as the robot's NCMs of motion (inspired by the analog term "normal vibrational modes" in molecular dynamics (Dresselhaus et al. 2007, chapter 8)). The qualifier "normal" underscores the orthogonality between the directions of motion associated with each NCM. Furthermore, when the dynamics of each NCM is independent of the other modes, the resultant decomposition of the dynamics is referred as dynamics harmonics analysis (DHA) (Ordoñez-Appraez et al. 2023).

To comprehend the decomposition of the dynamics, we begin by characterizing the block-diagonal structure of the joint-space generalized mass matrix in the isotypic basis. This structure is responsible for the independence of dynamics between the NCMs.

Block-diagonal structure of the joint-space generalized mass matrix Recall that the group representation $\rho_{\mathcal{M}} : \mathbb{G} \rightarrow \mathbb{GL}(\mathbb{R}^{n_j})$ implies that the joint-space configuration space \mathcal{M} is a symmetric space. Such spaces can be decomposed into a direct sum of isotypic subspaces, $\mathcal{M} := \mathcal{M}_1^{iso} \oplus^\perp \dots \oplus^\perp \mathcal{M}_{n_{iso}}^{iso}$, invariant under the action of \mathbb{G} (eq. (6)). That is, for $\mathbf{q}_{j_s} \in \mathcal{M}_k^{iso}$, then $g \triangleright \mathbf{q}_{j_s} \in \mathcal{M}_k^{iso}$ for all $g \in \mathbb{G}$. To achieve this, we identify an orthogonal change of basis $\mathbf{T} : \mathcal{M} \rightarrow \mathcal{M}$, which decomposes the joint-space group representation into a direct sum of the n_{iso} representations (eq. (5)), each acting on a specific subspace, i.e.,

$$\rho_{\mathcal{M}}^{iso}(g) := \rho_{\mathcal{M}_1^{iso}} \oplus \dots \oplus \rho_{\mathcal{M}_{n_{iso}}^{iso}} = \mathbf{T} [\rho_{\mathcal{M}}(g)] \mathbf{T}^\top, \quad (22)$$

where $\rho_{\mathcal{M}}^{iso}(g)$ denotes the group representation in the isotypic basis of \mathcal{M} , and each isotypic subspace \mathcal{M}_k^{iso} describes a unique subspace of symmetry-constrained robot configurations (a NCM), as depicted in fig. 8. Moreover, the constraints imposed on each subspace are solely determined by a subset of the symmetries of \mathbb{G} , associated with one of the unique irreducible representation $\bar{\rho}_k$ of the group \mathbb{G} . This is because, each $\rho_{\mathcal{M}_k^{iso}}$ is composed of m_k copies of a unique irreducible representation $\bar{\rho}_k$ of the group, i.e., $\rho_{\mathcal{M}_k^{iso}} \sim \bigoplus_p^{m_k} \bar{\rho}_k$. Refer to eq. (6).

The significance of this decomposition lies in the fact that the block-diagonal structure of the group representation leads to a similar structure in the joint-space generalized mass matrix $\bar{\mathbf{M}}(\mathbf{q}_{j_s})$ (eq. (14)).

Recall that a robot with a morphological symmetry group \mathbb{G} has a \mathbb{G} -equivariant generalized mass matrix (eq. (10)), and consequently, the joint-space mass matrix is also \mathbb{G} -equivariant. When we express this constraint in the isotypic basis, for all $g \in \mathbb{G}$ and $\mathbf{q}_{j_s} \in \mathcal{M}$, we obtain that the block-diagonal structure of $\rho_{\mathcal{M}}^{iso}$ (eq. (22)) enforces that all inertial terms between different isotypic subspaces are null:

$$\begin{aligned} \mathbf{T} \rho_{\mathcal{M}}(g) \bar{\mathbf{M}}(\mathbf{q}_{j_s}) \rho_{\mathcal{M}}(g)^{-1} \mathbf{T}^\top &= \mathbf{T} \bar{\mathbf{M}}(g \triangleright \mathbf{q}_{j_s}) \mathbf{T}^\top \\ \mathbf{T} \rho_{\mathcal{M}}(g) \mathbf{T} \mathbf{T}^\top \bar{\mathbf{M}}(\mathbf{q}_{j_s}) \mathbf{T}^\top \mathbf{T} \rho_{\mathcal{M}}(g)^{-1} \mathbf{T}^\top &= \mathbf{T} \bar{\mathbf{M}}(g \triangleright \mathbf{q}_{j_s}) \mathbf{T}^\top \\ \rho_{\mathcal{M}}^{iso}(g) \bar{\mathbf{M}}^{iso}(\mathbf{q}_{j_s}) \rho_{\mathcal{M}}^{iso}(g)^{-1} &= \bar{\mathbf{M}}^{iso}(g \triangleright \mathbf{q}_{j_s}) \\ \bigoplus_k^{n_{iso}} (\rho_{\mathcal{M}_k^{iso}}(g) \bar{\mathbf{M}}_k^{iso}(\mathbf{q}_{j_s}) \rho_{\mathcal{M}_k^{iso}}(g)^{-1}) &= \bigoplus_k^{n_{iso}} \bar{\mathbf{M}}_k^{iso}(g \triangleright \mathbf{q}_{j_s}). \end{aligned} \quad (23)$$

This essentially means that the \mathbb{G} -equivariance constraint breaks down the dynamics of the joint-space state into the independent dynamics of each isotypic subspace. In eq. (23), the block-diagonal $\bar{\mathbf{M}}^{iso}(\mathbf{q}_{j_s}) := \bigoplus_k^{n_{iso}} \bar{\mathbf{M}}_k^{iso}(\mathbf{q}_{j_s})$ represents the joint-space generalized mass matrix in the isotypic basis at configuration \mathbf{q}_{j_s} . Furthermore, the block $\bar{\mathbf{M}}_k^{iso}(\mathbf{q}_{j_s})$ signifies the isotypic subspace mass matrix at \mathbf{q}_{j_s} .

In the context of traditional sparsity exploitation algorithms in rigid body dynamics (Featherstone 2007), a similar decomposition is observed, in both ABA and RNEA algorithms,⁵ when dealing with two independent kinematic chains. Concretely, as the dynamics of each chain are independent, the inertial terms between the DoF of both chains are null. This property is leveraged by rigid body algorithms to reduce their computational complexity. In a similar vein, eq. (23) characterizes an independence of dynamics. However, in our case, this independence is not among individual DoF, but rather describes the independence of dynamics between the distinct symmetric types of synergistic motions controlled by each dimension of \mathcal{M} in the isotypic basis (fig. 8). Indeed, each dimension in the isotypic basis is transformed by \mathbf{T}^{-1} into a position configuration of multiple DoF in the original basis. Furthermore, the type of motion controlled is dependent on the symmetry constraints associated with each isotypic subspace.

Decomposing motions into a superposition of NCMs As discussed above, the decomposition of the joint-space mass matrix in the isotypic basis implies that we can break down any joint-space motion trajectory into a superposition of lower-dimensional synergistic motions governed by independent dynamics. In this section we provide a physical interpretation of such a decomposition.

Consider that the isotypic decomposition of the joint-space configuration implies that, with the change of coordinates \mathbf{T} , we can decompose any robot's joint-space state $(\mathbf{q}_{j_s}, \dot{\mathbf{q}}_{j_s})$ into its orthogonal components in each isotypic subspace, i.e.,

$$\begin{aligned} \mathbf{q}_{j_s}^{iso} &:= \mathbf{q}_{j_s}^{(1)} \oplus^\perp \dots \oplus^\perp \mathbf{q}_{j_s}^{(n_{iso})} = \mathbf{T} \mathbf{q}_{j_s}, \quad \text{and} \\ \dot{\mathbf{q}}_{j_s}^{iso} &:= \dot{\mathbf{q}}_{j_s}^{(1)} \oplus^\perp \dots \oplus^\perp \dot{\mathbf{q}}_{j_s}^{(n_{iso})} = \mathbf{T} \dot{\mathbf{q}}_{j_s}. \end{aligned} \quad (24)$$

Here, each $\mathbf{q}_{j_s}^{(k)} \in \mathcal{M}_k^{iso}$ and $\dot{\mathbf{q}}_{j_s}^{(k)} \in \mathcal{T}_{\mathbf{q}} \mathcal{M}_k^{iso}$ is the projection of the joint-space state in the isotypic subspace \mathcal{M}_k^{iso} and its tangent space $\mathcal{T}_{\mathbf{q}} \mathcal{M}_k^{iso}$, respectively (see fig. 8 and [animation 6](#)).

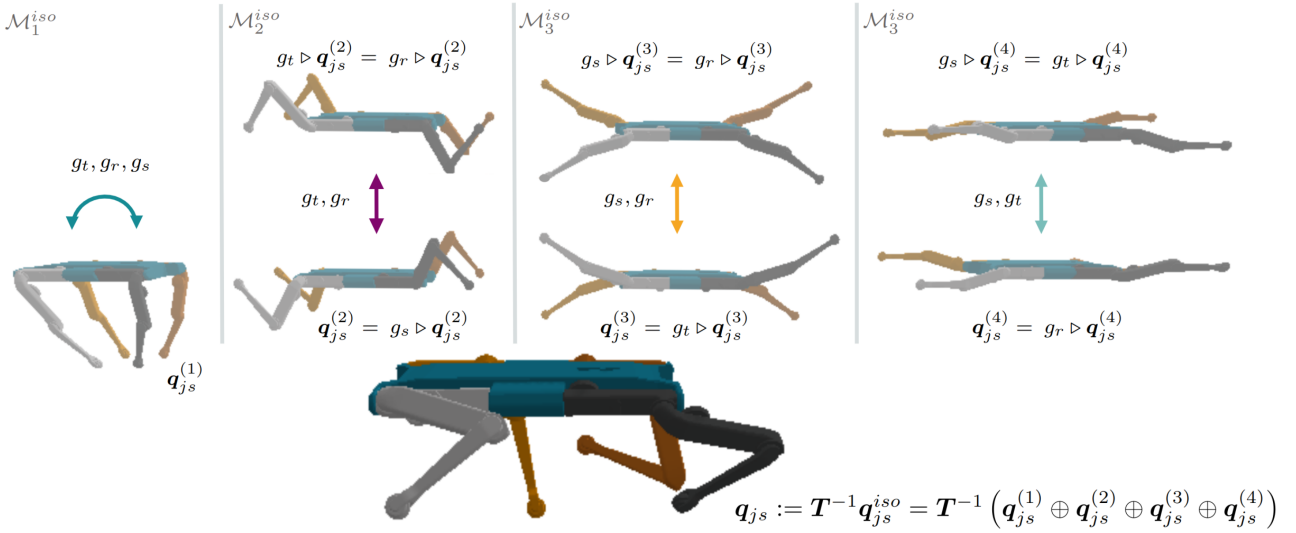


Figure 8. Isotypic decomposition of the joint-space configuration for the Solo quadruped robot (Griminger et al. 2020), taking into account its morphological symmetry group $\mathbb{G} = \mathbb{K}_4$ of order $|\mathbb{K}_4| = 4$ (see fig. 9a). After applying the change of basis T , the robot's 12-dimensional configuration space \mathcal{M} is decomposed into four orthogonal isotypic subspaces $[\mathcal{M}_k^{iso}]_{k=1}^4$, each of dimension 3. Consequently, any system configuration \mathbf{q}_{js} , or any velocity, acceleration, or force vector in $\mathcal{T}_q \mathcal{M}$, can be orthogonally decomposed into projections within each isotypic subspace. These subspaces are constrained to feature a unique subset of symmetry transformations from the group \mathbb{K}_4 . Thus, each subspace describes a range of symmetry-constrained robot's configurations, referred to as a normal configuration mode (NCM) of motion. The subspace \mathcal{M}_1^{iso} , associated with the symmetries of the trivial subgroup $\{e\} < \mathbb{K}_4$, represents the NCM of synchronized leg motions, where all legs share the same configuration. The remaining isotypic subspaces, \mathcal{M}_2^{iso} , \mathcal{M}_3^{iso} , and \mathcal{M}_4^{iso} , each constrained by symmetry subgroups isomorphic to a reflection group \mathbb{C}_2 , represent distinct patterns of synergistic motions. Specifically, \mathcal{M}_2^{iso} corresponds to synchronized left and right legs, \mathcal{M}_3^{iso} to synchronized front and back legs, and \mathcal{M}_4^{iso} to synchronized diagonally opposed legs.

Moreover, the equality between moving and inertial forces (see eq. (7)), implies that the block-diagonal structure of the joint-space generalized mass matrix results in a corresponding decomposition for the joint-space generalized momentum and forces:

$$\begin{aligned} \mathbf{T}(\overline{\mathbf{M}}(\mathbf{q}_{js})\dot{\mathbf{q}}_{js}) &:= \bigoplus_{k=1}^{n_{iso}} \overline{\mathbf{M}}_k^{iso}(\mathbf{q}_{js})\dot{\mathbf{q}}_{js}^{(k)}, \quad \text{and} \\ \mathbf{T}\overline{\boldsymbol{\tau}}(\mathbf{q}_{js}, \dot{\mathbf{q}}_{js}) &:= \bigoplus_{k=1}^{n_{iso}} \overline{\boldsymbol{\tau}}_k(\mathbf{q}_{js}, \dot{\mathbf{q}}_{js}), \end{aligned} \quad (25)$$

where $\overline{\boldsymbol{\tau}}(\mathbf{q}_{js}, \dot{\mathbf{q}}_{js})$ represents the joint-space generalized forces at the state $(\mathbf{q}_{js}, \dot{\mathbf{q}}_{js})$, and $\overline{\boldsymbol{\tau}}_k(\mathbf{q}_{js}, \dot{\mathbf{q}}_{js})$ denotes the projection of these forces in the isotypic subspace \mathcal{M}_k^{iso} . This result implies the joint-space dynamics is described by the independent dynamics of each isotypic subspace:

$$\overline{\mathbf{M}}_k^{iso}(\mathbf{q}_{js})\ddot{\mathbf{q}}_{js}^k = \overline{\boldsymbol{\tau}}_k(\mathbf{q}_{js}, \dot{\mathbf{q}}_{js}) \quad | \forall k \in [1, n_{iso}]. \quad (26)$$

To better understand this fact, consider a force vector $\mathbf{f} = [f_{\hat{x}}, f_{\hat{y}}, f_{\hat{z}}] \in \mathbb{R}^3$ acting on a specific body A . The force vector can be decomposed into orthogonal components aligned with the orthogonal basis vectors \hat{x} , \hat{y} , and \hat{z} of the Euclidean space \mathbb{R}^3 . Moreover, the instantaneous work done on the object, calculated as $\mathbf{f}^\top \dot{\mathbf{r}}_A$, is defined by the sum of the work done in each of these orthogonal directions of displacement. Analogously, in joint-space, the instantaneous work is computed from $\overline{\boldsymbol{\tau}}(\mathbf{q}_{js}, \dot{\mathbf{q}}_{js})^\top \dot{\mathbf{q}}_{js}$. Therefore, the decomposition in eq. (26), suggests that since the isotypic subspace describes orthogonal directions of displacement, the total work can be calculated by the sum of the work done in each of these orthogonal directions, i.e., in unconstrained directions of motion of each NCM. In other words, the direction of motion of a NCMs is orthogonal to the projection of the generalized force in all other isotypic subspaces (see fig. 8 and animation 6).

6 Applications of morphological symmetries

In this section, we present morphological symmetries as a physics informed geometric prior to be exploited in all data-driven applications of modeling, control, and estimation in robotics. We characterize how these symmetries can significantly enhance the performance of machine learning models and mitigate the challenges associated with data collection in robotics. In section 6.1, we present morphological symmetries as a technique for augmenting datasets comprised of the robots' proprioceptive and exteroceptive sensor measurements. Alternatively, in section 6.2, we show how to leverage morphological symmetries as constraints in learning and optimization processes, such as the optimization of the parameters of a neural network. Lastly, in section 6.3, we introduce the implications of DHA and the isotypic basis for analytical methods in control and estimation.

Overview Data-driven applications of supervised, unsupervised, and reinforcement learning rely on the approximation a target function $f \in \mathcal{F} : \mathcal{X} \rightarrow \mathcal{Y}$ using a model $f_\phi \in \mathcal{F}$ parameterized by learnable parameters ϕ , and a dataset $\mathbb{D} = \{(\mathbf{x}, \mathbf{y}), \dots\}$. Here, \mathcal{F} is the hypothesis function space, encompassing all functions mapping from the input space \mathcal{X} to the output space \mathcal{Y} .

In the field of robotics, both the input and output spaces usually comprise a combination of state and sensor data measurements. When the robotic system possesses a morphological symmetry group \mathbb{G} , these symmetries are imprinted in both the state and sensor data measurements. Consequently, both \mathcal{X} and \mathcal{Y} typically become symmetric

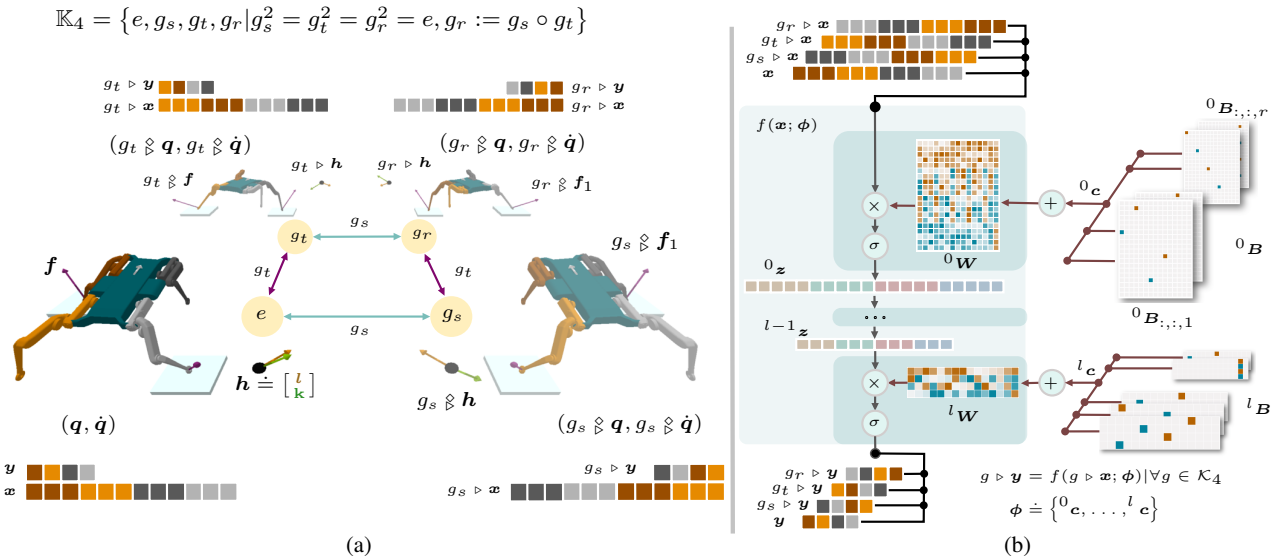


Figure 9. (a) Symmetries of the quadruped robot Solo (Griminger et al. 2020) and its sensor data measurements (see [animation 7](#)). The morphological symmetries are described by the Klein four-group \mathbb{K}_4 , which consists of two perpendicular reflections (g_s, g_t) and a 180° rotation (g_r) of space. These symmetry transformations influence the robot's state (q, \dot{q}) , resulting in the rotation/reflection of the state's associated proprioceptive sensor data measurements (contact forces $f \in \mathbb{R}^3$, centroidal linear $l \in \mathbb{R}^3$ and angular $k \in \mathbb{R}^3$ momenta), as well as exteroceptive measurements (contact points and contacts surface orientation $X_c \in \mathbb{SE}_3$). (b) Diagram depicting a \mathbb{K}_4 -equivariant neural network that processes the state and sensor data measurements of the Solo robot, x , and outputs the binary foot contact states for each leg, y . The network's \mathbb{G} -equivariance is achieved by constraining each linear layer's weight matrix $^iW \in \mathbb{R}^{n \times m}$ to the space of \mathbb{G} -equivariant matrices, such that $^iW = g \diamond ^iW$ for all $g \in \mathbb{K}_4$. This constraint reduces the layer's trainable parameters to the vector of coefficients $^ic \in \mathbb{R}^p$, which mixes the $p < mn$ basis vectors of the layer's space of \mathbb{G} -equivariant matrices.

vector spaces, and the target function f transitions into a \mathbb{G} -invariant or \mathbb{G} -equivariant map, as outlined in eq. (1). We can exploit this bias either through the use of data augmentation or by enforcing equivariance/invariance constraints on the machine learning model.

6.1 Data augmentation

As discussed earlier, a morphological symmetry refers to a robotic system's ability to replicate a Euclidean isometry through a feasible state transformation. This isometry can be interpreted as a transformation of both the system's state and the robot's operational environment. Considering that any rotation, reflection, or translation of the world results in an equally plausible operational environment, it follows that any proprioceptive and exteroceptive sensor data measurement, captured by the system at a given state (q, \dot{q}) , can be related to a measurement taken by the system at the transformed state $(g \otimes q, g \otimes \dot{q})$ within the transformed operational environment as depicted in fig. 9a.

Consider a dataset $\mathbb{D} = \{(x_0, y_0), \dots, (x_{|\mathbb{D}|}, y_{|\mathbb{D}|})\}$ derived from the robot's operation in either a simulated or real-world environment. Each data point (x, y) may comprise a combination of state (q, \dot{q}) measurements and associated proprioceptive/exteroceptive sensor data measurements, such as contact forces, tactile sensing, height maps, depth maps, joint torques, etc (see fig. 9a).

By leveraging the robot's morphological symmetry group \mathbb{G} , we can synthetically generate $|\mathbb{G}|$ samples per data point. This is achieved by considering the orbit of symmetric measurements $\mathbb{G}(x, y) = \{(g \triangleright x, g \triangleright y) | \forall g \in \mathbb{G}\}$, effectively increasing the dataset size to $|\mathbb{G}||\mathbb{D}|$, as depicted in fig. 9a. Therefore, this method serves as a form of data augmentation, assuming the generated sample belongs

to the same data distribution as the original dataset. In other words, if the probability of encountering the data point (x, y) during the robot's normal operation should be the same as the probability of encountering $(g \triangleright x, g \triangleright y)$. For example, for every minute of recorded data from the Mini Cheetah robot with $|\mathbb{G}| = 8$, we can augment the dataset with an additional 7 minutes of recordings by applying the symmetries to the data (see animation 1).

To augment the data, we need to define the action of a symmetry on the input/output spaces \mathcal{X} and \mathcal{Y} . This involves identifying the group representations $\rho_x(g) \in \mathbb{GL}(\mathcal{X})$ and $\rho_y(g) \in \mathbb{GL}(\mathcal{Y})$, which allows us to apply the group actions $g \triangleright x := \rho_x(g)x$ and $g \triangleright y := \rho_y(g)y$. Since \mathcal{X} and \mathcal{Y} are comprised of proprioceptive/exteroceptive sensor data measurements, these group representations are constructed from direct sums/products of the group representations we identified in sections 2, 4 and 5.

Exteroceptive measurements These measurements can be represented as individual points, and spatial vectors, or a combination thereof. They may encompass contact points, contact forces, terrain or surface normals, depth images, and the positions and orientations of bodies in space. To transform these measurements, we employ the group representations $\rho_{\mathbb{R}^{d+1}}$ and $\rho_{\mathbb{R}^d}$ (or direct sums/products of these representations). These represent the rotation/reflection or translation associated with each $g \in \mathbb{G}$, as detailed in eq. (3).

Proprioceptive measurements Proprioceptive measurements can often be represented as geometric quantities in \mathbb{R}^d . Examples include contact points, end-effector positions/velocities. To transform these we use $\rho_{\mathbb{R}^{d+1}}$ and $\rho_{\mathbb{R}^d}$, as above. Alternatively, proprioceptive measurements can

be points in the system's joint-space \mathcal{M} and \mathcal{TQ} spaces, such as joint positions/velocities/accelerations/torques. To transform these measurements, we employ the group representations $\rho_{\mathcal{M}}, \rho_{\mathcal{TQ}}$ (characterized in section 5). When the measurements are associated with one of the robot's n_k unique kinematic branches, such as leg contact states in a locomoting system (see fig. 9) or the end-effector position of limb, we utilize the permutation representations $[\rho_{s_i}]_{i=1}^{n_k}$.

The above-mentioned representations allow us to apply an appropriate reordering of measurements, according to the permutations of the branches (see section 5.3.1). For instance, consider the task of augmenting the vector composed of the three body velocities of the last body of each limb of the robot depicted in fig. 6b. This vector, denoted as $\mathbf{x} = [\dot{\mathbf{r}}_{l,1,2}^T, \dot{\mathbf{r}}_{l,2,2}^T, \dot{\mathbf{r}}_{l,3,2}^T]^T \in \mathbb{R}^9$, can be transformed using the group representation for vectors in \mathbb{R}^d (i.e., $\rho_{\mathbb{R}^d}$) and the limb's permutation representation ρ_{s_i} . The resulting representation $\rho_{\mathcal{X}} := \rho_{s_i} \otimes \rho_{\mathbb{R}^d}$ is obtained in a manner analogous to the process outlined in eq. (20).

6.2 Equivariant/Invariant function approximation

In robotics, the target function $f \in \mathcal{F} : \mathcal{X} \rightarrow \mathcal{Y}$ we aim to approximate is often a \mathbb{G} -invariant or \mathbb{G} -equivariant map. This constraint narrows the hypothesis space \mathcal{F} to either the space of \mathbb{G} -invariant functions $\mathcal{F}_{\mathbb{G}}^{inv}$ or \mathbb{G} -equivariant functions $\mathcal{F}_{\mathbb{G}}^{eq}$ (Weiler et al. 2023). As introduced above, these are defined as:

$$\begin{aligned} \mathcal{F}_{\mathbb{G}}^{inv} &= \{f \in \mathcal{F} \mid \mathbf{y} = f(g \triangleright \mathbf{x}), \forall g \in \mathbb{G}\}, \\ \mathcal{F}_{\mathbb{G}}^{eq} &= \{f \in \mathcal{F} \mid g \triangleright \mathbf{y} = f(g \triangleright \mathbf{x}), \forall g \in \mathbb{G}\}. \end{aligned}$$

Therefore, an alternative to data augmentation when approximating \mathbb{G} -invariant/equivariant functions is to constrain the function space of the machine learning model. This can be achieved by ensuring that $f_{\phi} \in \mathcal{F}_{\mathbb{G}}^{inv}$ or $f_{\phi} \in \mathcal{F}_{\mathbb{G}}^{eq}$. While this constraint reduces the model's expressivity by limiting the types of functions it can represent (Bronstein et al. 2021), it also enhances the model's generalization capabilities beyond the training distribution and improves sample efficiency. Below, we include examples of \mathbb{G} -equivariant and \mathbb{G} -invariant functions in robotic systems with morphological symmetry group \mathbb{G} .

\mathbb{G} -equivariant functions Examples of \mathbb{G} -equivariant functions in robotics include the forward and inverse dynamics, as outlined in eq. (9), and the generalized mass matrix function, as per eq. (10). Other examples include the robot's positional and rotational Jacobians, collectively represented as a map $J : \mathcal{Q} \times \mathcal{TQ} \rightarrow \mathfrak{se}_d$ introduced in eq. (21) (Wieber (2006)). The inverse and forward kinematics functions, defined as the maps $f_{ik} : \mathbb{E}_d \rightarrow \mathcal{Q}$ and $f_{fk} : \mathcal{Q} \rightarrow \mathbb{E}_d$, respectively, also fall into this category. Additionally, practical non-analytical functions, such as contact location detection (see fig. 9), can also be considered \mathbb{G} -equivariant.

\mathbb{G} -Invariant Functions Examples of \mathbb{G} -invariant functions in robotics include the robot's kinetic energy $T : \mathcal{Q} \times \mathcal{TQ} \rightarrow \mathbb{R}$ and potential energy $V : \mathcal{Q} \rightarrow \mathbb{R}$, as outlined in definition 1. Additionally, practical non-analytical functions such as the detection of external disturbance and emergency stop scenarios also fit into this category.

Optimal control and reinforcement learning In optimal control and reinforcement learning settings, the control policy $\pi : \mathcal{S} \rightarrow \mathcal{A}$ is constrained to be \mathbb{G} -equivariant functions when both of the Markov decision process (MDP) state \mathcal{S} and action \mathcal{A} spaces are symmetric spaces, and the reward function $r : \mathcal{S} \times \mathcal{A} \rightarrow \mathbb{R}$ is \mathbb{G} -invariant (Zinkevich and Balch 2001; Wang et al. 2022a). This is particularly pertinent for robots with morphological symmetries, as the MDP state space is typically defined as $\mathcal{S} := \mathcal{Q} \times \mathcal{TQ} \times \mathcal{X}_d$ and \mathcal{A} is usually a subspace of \mathcal{TQ} . Here, \mathcal{X}_d represents a space of relevant sensor data measurements for control, such as perception sensor measurements and contact states. Therefore, both \mathcal{S} and \mathcal{A} are typically symmetric spaces.

Most reward functions are \mathbb{G} -invariant in practice, as these functions are often defined in terms of distances in Euclidean space and/or configuration space, such as, distance to target point/configuration (Wang et al. 2022b; Brehmer et al. 2023). These measurements remain invariant under Euclidean isometries and morphological symmetries. Moreover, the \mathbb{G} -invariance of the reward functions translates to the \mathbb{G} -invariance of the value $V_{\pi} : \mathcal{S} \rightarrow \mathbb{R}$, and action-value function $Q_{\pi} : \mathcal{S} \times \mathcal{A} \rightarrow \mathbb{R}$ (Zinkevich and Balch 2001). These are the fundamental functions upon which optimal control and reinforcement learning algorithms are built (Sutton and Barto 2018; Zinkevich and Balch 2001). Several works have provided empirical evidence of the benefits of symmetry exploitation in approximating these functions (Brehmer et al. 2024; Rezaei-Shoshtari et al. 2022; Wang et al. 2022a; Weissenbacher et al. 2022; Mondal et al. 2022; Van der Pol et al. 2020; Finzi et al. 2021; Wang et al. 2022c).

6.3 Dynamics Harmonics Analysis

As detailed in section 5.5, the joint-space dynamics of a robotic system with morphological symmetries can be decomposed into a superposition of lower-dimensional NCM. This decomposition is done by applying an invertible change of basis T to \mathcal{M} , as referenced in eq. (22) and fig. 8. The invertibility of T allows for seamless transitions between the isotypic and the canonical basis, where each dimension represents the position of a single DoF. Certain operations, such as mass matrix inversion and control policy optimization, can benefit from being performed in the isotypic basis.

The block-diagonal structure of the joint-space generalized mass matrix suggests that its inversion, required to compute the system's inverse dynamics, can be decomposed into the (potentially parallel) inversion of $n_{i,so}$ lower-dimensional mass matrices per isotypic subspace (refer to eq. (23)). This results in a gain in computational complexity (Eves 1980; Mastalli et al. 2023). This technique bears similarity with methods exploiting the sparsity of the mass matrix induced by the kinematic structure (Featherstone 2007; Carpentier et al. 2021).

Moreover, the isotypic basis of the robot's joint space provides a control action space where each dimension governs a specific synergistic motion involving multiple DoF of the robot. Each isotypic subspace encodes the space of normal harmonic motion (i.e., lower-dimensional synergistic symmetric motions with independent dynamics) (refer to section 5.5 and fig. 8). This conceptual decomposition aligns with theories in biomechanics and motor control

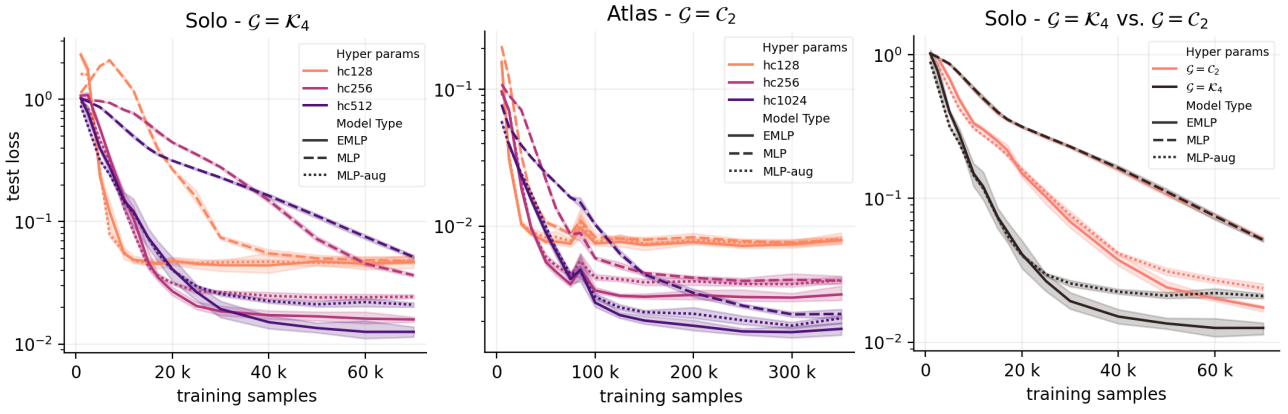


Figure 10. Centroidal estimation results comparing MLP, MLP_{aug}, and eMLP models. Left and Middle: Test set sample efficiency of model variants with different capacities (number of neurons hc in hidden layers) for the Solo and Atlas robots. Right: Sample efficiency for the Solo robot with models having $hc = 512$, when exploiting $\mathbb{G} = \mathbb{K}_4$ (sagittal and traversal symmetries) and $\mathbb{G} = \mathbb{C}_2 = e, g[s] \subset \mathbb{K}_4$ (only sagittal symmetry). The plots depict the average and standard deviation across 10 seeds.

(Scholz and Schöner 1999; Feldman and Levin 2009; Ijspeert 2008), which sustain that the control of a high-DoF system is not achieved by individually controlling each DoF. Instead, it is controlled as the superposition of several lower-dimensional synergistic motions, often referred to in robotics as dynamic motion primitives (DMPs) (Schaal et al. 2003). In this context, the basis of NCM of robotic systems with morphological symmetry groups \mathbb{G} can be interpreted as a basis of *symmetric* DMPs. This basis is derived analytically from the knowledge of the system’s morphological symmetries, providing a systematic way to identify these lower-dimensional synergistic motions for arbitrary symmetric systems.

7 Experiments

In this section, we empirically demonstrate the benefits of leveraging morphological symmetries in data-driven methods. We examine the impact of symmetry exploitation on the generalization and sample efficiency of neural network-based machine learning models. Specifically, we focus on two cases: data augmentation and equivariance/invariance constraints. To do so, we conducted synthetic and real-world experiments involving the approximation of several \mathbb{G} -invariant and \mathbb{G} -equivariant functions. These are regression and classification problems in supervised learning.

We conduct a synthetic experiment that involves a regression problem, with the goal of approximating the \mathbb{G} -equivariant function that computes the system’s centroidal momentum, as detailed in section 7.1. In addition, we present a real-world classification problem in section 7.2, which utilizes a dataset of the Mini Cheetah quadruped robot’s locomotion across various terrains and using different gaits (Lin et al. 2021). Specifically, our focus is on approximating the \mathbb{G} -equivariant static-friction-regime contact detection function, a crucial component in leg odometry and state estimation.

To approximate these functions, we trained a conventional neural network model $f_\phi \in \mathcal{F}$ on a dataset $\mathbb{D} = \{(\mathbf{x}_0, \mathbf{y}_0), \dots, (\mathbf{x}_{|\mathbb{D}|}, \mathbf{y}_{|\mathbb{D}|})\}$, which was partitioned into training, validation, and testing sets (70%, 15%, and 15% of $|\mathbb{D}|$, respectively). We compared this model against another trained on an augmented training dataset of size $0.7|\mathbb{G}||\mathbb{D}|$.

Additionally, we compared against a \mathbb{G} -equivariant model $f_{\phi_{eq}} \in \mathcal{F}_{\mathbb{G}}^{eq}$ (section 6.2). Both of these models leverage the robot’s morphological symmetry group (section 6).

Finally, to motivate our finding in section 6.3, we present in section 7.3 how DHA can be used to characterize the lower-dimensional synergistic nature of the dynamics of legged locomotion in quadruped robots.

7.1 Centroidal momenta estimation \mathbb{G} -equivariant regression

We approximated the robot’s linear $\mathbf{l} \in \mathbb{R}^3$ and angular $\mathbf{k} \in \mathbb{R}^3$ momentum as a function of the system’s state $(\mathbf{q}, \dot{\mathbf{q}})$. This involved computing the momentum of each of the robot’s n_b bodies and aggregating these relative to the state-dependent CoM location. As introduced above, the centroidal momentum is a highly non-linear and \mathbb{G} -equivariant function reliant on the robot’s kinematic and dynamic parameters with morphological symmetries (refer to section 5 and fig. 9a):

$$g \triangleright \mathbf{h} = \mathbf{A}_C(g \otimes \mathbf{q})g \triangleright \dot{\mathbf{q}} \quad (27)$$

$$|g \triangleright \mathbf{h} := \rho_{\mathcal{H}}(g)\mathbf{h} = \begin{bmatrix} \mathbf{R}_g & \mathbf{0} \\ \mathbf{0} & |\mathbf{R}_g| \mathbf{R}_g \end{bmatrix} \begin{bmatrix} \mathbf{l} \\ \mathbf{k} \end{bmatrix}, \forall g \in \mathbb{G},$$

where $\mathbf{h} \in \mathcal{H} \subseteq \mathbb{R}^6$ denotes the stacked linear and angular momentum components, and \mathbf{A}_C is the state-dependent centroidal momentum matrix (CMM) function introduced by Orin et al. (2013). The group representation $\rho_{\mathcal{H}}$ outlines the corresponding rotation or reflection of these momentum components. Importantly, the action on the flat angular momentum, $|\mathbf{R}_g| \mathbf{R}_g$,⁸ signifies the necessary change of sign for axial or pseudovector quantities in the event of a reflection (Quigley 1973), as depicted in fig. 9a.

To approximate this function, we utilized a standard multi layer perceptron (MLP) model $f_\phi \in \mathcal{F} : \mathcal{Q} \times \mathcal{TQ} \rightarrow \mathcal{H}$, trained using a synthetic dataset $\mathbb{D} = \{((\mathbf{q}, \dot{\mathbf{q}}), \mathbf{h}), \dots\}$, generated with eq. (27) and PINOCCHIO (Carpentier et al. 2019). We compared with the model trained using the augmented dataset MLP with data augmentation (MLP_{aug}), and a \mathbb{G} -equivariant version of the model $f_{\phi_{eq}} \in \mathcal{F}_{\mathbb{G}}^{eq}$ (refer to section 6.2), denoted as equivariant multi layer perceptron (eMLP). We tested two robots: Atlas, a 32-DoF humanoid robot with $\mathbb{G} = \mathbb{C}_2$ (see fig. 3), and Solo, a 12-DoF quadruped robot with $\mathbb{G} = \mathbb{K}_4$ (see fig. 9).

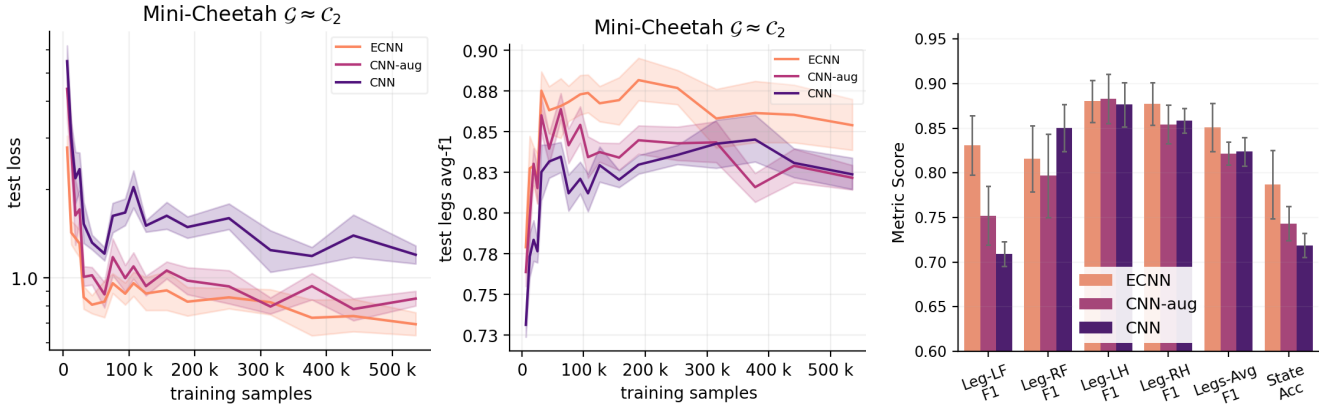


Figure 11. Static-Friction-Regime contact detection results comparing convolutional neural network (CNN), CNN trained with data augmentation (CNN_{aug}), and equivariant CNN (eCNN). Left: Sample efficiency in log-log scale. Middle: Average legs F1-score. Right: Classification metrics on test set performance of models trained with the entire training set. The selected metrics include contact-state ($\mathbf{y} \in \mathbb{R}^{16}$) accuracy (Acc) and f1-score (F1) for each leg binary contact state. Due to the sagittal symmetry of the robot, the left front (LF) and right front (RF) legs are expected to be symmetric, as well as the left hind (LH) and right hind (RH) legs. F1-score is presented considering the class imbalanced nature of the dataset. The reported values represent the average and standard deviation across 8 different seeds.

In fig. 10-left/middle, we compare the performance of several MLP models with varying numbers of trainable parameters, against their counterparts using data augmentation MLP_{aug} and \mathbb{G} -equivariance constraints eMLP. Across both robots and all model capacities, eMLP and MLP-Aug outperform MLP in terms of sample efficiency (better generalization with fewer data) and robustness to overfitting when training data is limited. Among the eMLP and MLP_{aug} variants, the models with the lowest number of trainable parameters exhibit similar sample complexity and performance, but as the model’s capacity increases, the eMLP model reaches a superior sample efficiency and generalization. In addition, fig. 10-right shows a comparison for the Solo robot, evaluating the performance of the model variants when exploiting either the entire symmetry group (\mathbb{K}_4) or a subgroup of the true symmetry group ($\mathbb{C}_2 \subset \mathbb{K}_4$). The results indicate that sample efficiency and generalization capacity increase with the number of *true* symmetries of the data exploited.

7.2 Static-friction-regime contact detection \mathbb{G} -equivariant classification

We aim to approximate a function detecting the static-friction-regime binary contact state of the four legs of the Mini Cheetah quadruped robot, with symmetry group $\mathbb{G} = \mathbb{K}_4 \times \mathbb{C}_2$. This function’s inputs are the history of the state and proprioceptive sensor data measurements and outputs are binary variables per leg indicating whether the robot’s leg is in a static-friction-regime state or in a non-contact or slipping state. These categorical estimated measurements are fundamental in state estimation pipelines dependent on leg odometry (e.g., Camurri et al. 2017; Lin et al. 2021) and legged locomotion control (e.g., Mastalli et al. 2020b; Lee et al. 2020; Corbères et al. 2024).

The dataset $\mathbb{D} = \{(\mathbf{x}_t]_{t=0}^{-150}, \mathbf{y}_t, \dots\}$, first introduced by Lin et al. (2021), comprises samples containing a categorical variable $\mathbf{y} \in \mathbb{R}^{16}$. This variable represents the ground truth system’s contact state among the 16 different combinations of each of the 4 legs’ possible binary contact states. Each sample also includes a history of the past 150

frames of a vector of proprioceptive sensor data measurements $\mathbf{x} = [\mathbf{q}_{js}, \dot{\mathbf{q}}_{js}, {}^B \ddot{\mathbf{r}}_B, {}^B \boldsymbol{\omega}_B, {}^B \mathbf{r}_{feet}, {}^B \dot{\mathbf{r}}_{feet}] \in \mathcal{X} \subseteq \mathbb{R}^{54}$. Here, $\mathbf{q}_{js} \in \mathcal{M} \subseteq \mathbb{R}^{12}$ and $\dot{\mathbf{q}}_{js} \in \mathcal{T}_q \mathcal{M} \subseteq \mathbb{R}^{12}$ denote the robot’s joint space position and velocity generalized coordinates, ${}^B \ddot{\mathbf{r}}_B$ and ${}^B \boldsymbol{\omega}_B \in \mathbb{R}^3$ represent the robot’s base linear acceleration and angular velocity, and ${}^B \mathbf{r}_{feet} = [{}^B \mathbf{r}_{RF}, {}^B \mathbf{r}_{LF}, {}^B \mathbf{r}_{RH}, {}^B \mathbf{r}_{LH}] \in \mathcal{X}_{feet} \subseteq \mathbb{R}^{12}$ and ${}^B \dot{\mathbf{r}}_{feet} = [{}^B \dot{\mathbf{r}}_{RF}, {}^B \dot{\mathbf{r}}_{LF}, {}^B \dot{\mathbf{r}}_{RH}, {}^B \dot{\mathbf{r}}_{LH}] \in \mathcal{X}_{feet} \subseteq \mathbb{R}^{12}$ are the positions and velocities of each of the four legs’ feet, respectively.

The ground truth contact state is estimated offline using a non-causal algorithm, i.e., a function dependent on both past and future proprioceptive measurements. The experiment’s objective is to train a model to predict the contact state using only past proprioceptive data. Our unconstrained model $f_\phi \in \mathcal{F} : \mathcal{X} \rightarrow \mathcal{Y}$ is the original CNN architecture from Lin et al. (2021). We compare this model against the CNN_{aug} and the eCNN, denoted $f_{\phi_{eq}} \in \mathcal{F}_{\mathbb{G}}^{eq}$.

Determining the input and output group representations

$\rho_{\mathcal{X}}$ and $\rho_{\mathcal{Y}}$ To define the group action on the input space, we proceeded as detailed in section 5.3 and identified the labels $\mathbb{S}_{leg} = \{RF, LF, RH, LH\}$ of the four instances of the unique kinematic branches along with the label’s permutation representation $\rho_{\mathbb{S}_{leg}}$. These labels describe the change of roles of the legs under a symmetry transformation (see fig. 1). Since the position and velocity measurements in ${}^B \mathbf{r}_{feet}$ and ${}^B \dot{\mathbf{r}}_{feet}$ are associated with each leg, we rotated/reflected these measurements and permuted the robot’s legs to define the symmetry transformations, i.e., $\rho_{\mathcal{X}_{feet}} := \rho_{\mathbb{S}_{leg}} \otimes \rho_{\mathbb{R}^3}$. This enabled us to define the input space group representation as $\rho_{\mathcal{X}} := \rho_{\mathcal{M}} \oplus \rho_{\mathcal{T}_q \mathcal{M}} \oplus \rho_{\mathbb{R}^3} \oplus \rho_{\mathbb{R}^3} \oplus \rho_{\mathcal{X}_{feet}} \oplus \rho_{\mathcal{X}_{feet}}$.

The sampling efficiency and average leg contact state classification results are depicted in fig. 11-left-middle. The equivariant model eCNN has superior generalization performance and robustness to dataset biases compared to the unconstrained models. Following eCNN, CNN_{aug} exhibits better performance than the original CNN. In fig. 11-right, we report the classification metrics of the test set when using the entire training data. The eCNN model outperforms both CNN_{aug} and CNN in contact state classification

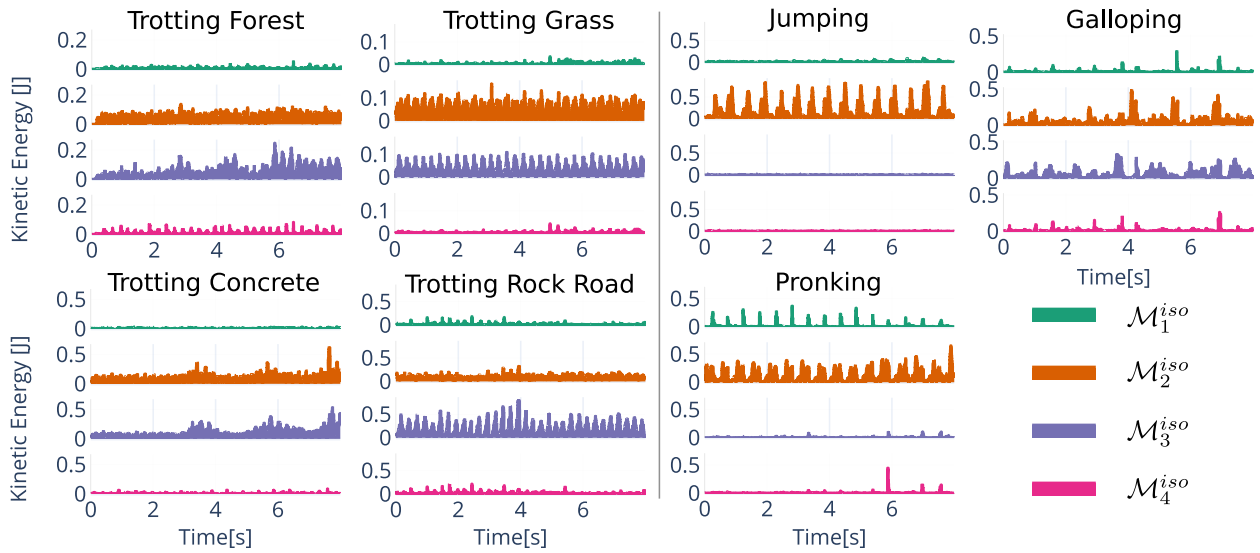


Figure 12. Decomposition of the dynamics of locomotion of the Mini Cheetah robot as a superposition of lower-dimensional NCM. Each robot’s dynamic behavior is characterized by their projections onto the isotypic spaces $\mathcal{M}_1^{iso}, \mathcal{M}_2^{iso}, \mathcal{M}_3^{iso}, \mathcal{M}_4^{iso} \subseteq \mathbb{R}^3$. The relevance of each isotypic subspace in characterizing different locomotion gaits is quantified by computing the joint space kinetic energy of the state projections. **Left:** The trotting gait dynamics on forest, grass, concrete, road with rocks terrains primarily evolve in the $\mathcal{M}_2^{iso} \times \mathcal{M}_3^{iso} \in \mathbb{R}^6$ subspace, as indicated by the kinetic energy distribution. **Right:** The jumping, pronking, gaits on asphalt terrain mainly evolve in \mathcal{M}_2^{iso} and $\mathcal{M}_1^{iso} \times \mathcal{M}_2^{iso} \in \mathbb{R}^6$ subspaces, respectively, while the galloping gait dynamics periodically evolve in all isotypic subspaces.

and average leg contact detection. Notably, exploiting symmetries held mitigate suboptimal asymmetries in the models, preventing them from favoring the classification of one leg over others (observe legs LF and RF in fig. 11-right).

7.3 Dynamics harmonics analysis applied to the locomotion of a quadruped robot

In this experiment, we utilize the basis of NCM of the Mini Cheetah robot’s joint-space to characterize various locomotion gaits, across different terrains, by decomposing these behaviors into a superposition of lower-dimensional NCM (refer to section 5.5).

Specifically, we took real-world joint-space motion trajectories $[(\mathbf{q}_{j_s,t}, \dot{\mathbf{q}}_{j_s,t})]_{t \in \mathbb{T}}$, collected over a certain time span \mathbb{T} from the dataset in section 7.2, and projected them onto the robot’s isotypic subspaces. This projection is accomplished by applying a change of basis \mathbf{T} to \mathcal{M} , as outlined in eq. (24). The result are n_{iso} lower-dimensional trajectories $[(\mathbf{q}_{j_s,t}^{(k)}, \dot{\mathbf{q}}_{j_s,t}^{(k)})]_{t \in \mathbb{T}}$ for each of the n_{iso} isotypic subspaces, representing symmetry constrained state trajectories. For instance, see an example of the decomposition of a motion trajectory into four lower-dimensional trajectories in animation 6.

To identify which isotypic subspaces are relevant in characterizing the different locomotion gaits, we take each of these lower-dimensional trajectories and independently compute their joint space kinetic energy. This value is a proxy indicating how much of the original trajectories generalized momentum and forces (eq. (26)), is explained by the isotypic subspace. In fig. 12, we show how this decomposition can be used to identify the lower-dimensional nature of the trotting, jumping, pronking, and galloping gaits of the Mini Cheetah robot. Each of these gaits primarily evolves in a 3 or 6-dimensional subspace of the joint-space composed of one or two isotypic subspaces. Furthermore, the less relevant subspaces for each gait appear to be exited only

temporarily during disturbance rejection. Interestingly, even when the terrain changes, the distribution of kinetic energy between isotypic spaces remains unaffected, as depicted in fig. 12-left for a trotting gait. This indicates that to control these dynamic behaviors, the bulk of the control policy optimization is expected to be performed in the relevant isotypic subspaces.

8 Conclusions

This work presents a framework based on group and representation theory for leveraging morphological symmetries in robotics. These symmetries, inherent in a robot’s body structure, correspond to symmetries in mass distribution and the duplication of kinematic branches. We illustrated how these symmetries extend to the robot’s state space and both proprioceptive and exteroceptive measurements, resulting in the equivariance of the robot’s equations of motion and optimal control policies. Furthermore, we revealed the potential of these symmetries to enhance both data-driven and analytical approaches for modeling, control, and estimation in robotics.

In the context of data-driven methods, we showed how morphological symmetries can be leveraged to boost a machine learning model’s sample efficiency and generalization capabilities. This underscores their value in addressing the robustness and reliability requirements that are critical for deploying data-driven models in robotics applications, where the challenges of data collection are particularly pronounced. The enhancement of the model can be realized either through data augmentation or by enforcing equivariance/invariance constraints on the models. We provided empirical evidence of these benefits through two experiments—a synthetic regression and a real-world classification problems— involving both a bipedal and a quadrupedal robot.

In the context of analytical methods, we leveraged morphological symmetries to simplify the modeling and control of symmetric robotic systems. Specifically, we used abstract harmonic analysis to identify the block-diagonal structure of a robot's joint-space mass matrix, leading to the decomposition of the robot's dynamics into a superposition the independent dynamics of several lower-dimensional synergistic symmetry-constrained robot motions. This method, inspired by the use of harmonic analysis in particle physics, is introduced in robotics by the term dynamics harmonics analysis (DHA). We have demonstrated the relevance of this decomposition in the context of legged locomotion, by identifying the low-dimensional synergistic nature of the dynamics of locomotion of the Mini Cheetah robot, providing insights into the lower-dimensional spaces relevant for the motion control per each gait type.

Discussion and future work

We identified three relevant directions of exploration of the implications of morphological symmetries

Optimization The use of DHA (section 5.5), facilitates the parallel optimization on each of the orthogonal isotypic subspaces of \mathcal{M} in trajectory optimization methods. Notably, this decomposition can be leveraged in the iLQR (Li and Todorov 2004) and DDP (Mayne 1966) algorithms, which play a crucial role in trajectory optimization for control and estimation (Tassa et al. 2014; Mastalli et al. 2020a; Alessandri et al. 2003; Kobilarov et al. 2015).

Computational Design Morphological symmetries provide substantial advantages for both data-driven and analytical methods in modeling, control, and estimation in robotics. The extent of these benefits is proportional to the order and structure of the symmetry group. This underscores the potential use of computational design in optimizing a system's morphology to exploit these implications.

Continuum, Soft, and Modular Robots Morphological symmetries are a common feature in soft, continuum, and modular robots. These robots often lack analytical solutions for forward/inverse kinematics/dynamics functions, necessitating the use of data-driven methods for function approximation. The presence of morphological symmetries in these robots imposes \mathbb{G} -equivariant/invariance constraints on these target functions. This provides a means to integrate the invariances inherent in Newtonian physics into the modeling and control of these robot types.

Notes

1. Morphological symmetry group of the Mini Cheetah robot $\mathbb{G} = \mathbb{C}_2 \times \mathbb{C}_2 \times \mathbb{C}_2$: See animation at <https://bit.ly/MiniCheetah-MorphoSymm>
2. Equivariant temporal evolution of symmetric states of the Mini Cheetah robot See animation at <https://bit.ly/MiniCheetah-SymmetricTemporalEvolution>
3. Open access repository: github.com/Danfoa/MorphoSymm
4. The mechanical work function $U : \mathcal{Q} \times \mathcal{T}\mathcal{Q} \rightarrow \mathbb{R}_+$ encompasses the system's potential energy (determined by all conservative forces acting on the system) and the work done by

all non-conservative forces, such as friction, control actions, contact forces, external disturbances.

5. ABA stands for Articulated Body Algorithm, while RNEA stands for Recursive-Newton Euler algorithm (Featherstone 2007).
6. Harmonic analysis of the Mini Cheetah robot: Animation online in the <https://bit.ly/MiniCheetah-DHA-Trot-Concrete>
7. Morphological Symmetry group of the Solo robot $\mathbb{G} = \mathbb{K}_4$: See animation online at <https://bit.ly/Solo-MorphoSymm-Klein4>
8. The action of a rotation/reflection on a flat pseudovector (or axial vector) \mathbf{k} is defined as $g \triangleright \mathbf{k} := |\mathbf{R}_g| \mathbf{R}_g \mathbf{k}$. This is equivalent to the symmetry action described in eq. (11), in which axial vectors is represented as a member of the special Orthogonal group Lie algebra \mathfrak{so}_d , that is, as a skew-symmetric representation of the axial vector. In this form the group action is defined as $g \triangleright [\mathbf{k}]_{\times} := \mathbf{R}_g \diamond [\mathbf{k}]_{\times} = \mathbf{R}_g [\mathbf{k}]_{\times} \mathbf{R}_g^T$

References

- Alessandri A, Baglietto M and Battistelli G (2003) Receding-horizon estimation for discrete-time linear systems. *IEEE Transactions on Automatic Control* 48.
- Bietti A, Venturi L and Bruna J (2021) On the sample complexity of learning under invariance and geometric stability. *arXiv preprint arXiv:2106.07148*.
- Brehmer J, Bose J, De Haan P and Cohen TS (2024) Edgi: Equivariant diffusion for planning with embodied agents. *Advances in Neural Information Processing Systems* 36.
- Brehmer J, De Haan P, Behrens S and Cohen T (2023) Geometric algebra transformers. *arXiv preprint arXiv:2305.18415*.
- Bronstein MM, Bruna J, Cohen T and Veličković P (2021) Geometric deep learning: Grids, groups, graphs, geodesics, and gauges. *arXiv preprint arXiv:2104.13478*.
- Camurri M, Fallon M, Bazeille S, Radulescu A, Barasuol V, Caldwell DG and Semini C (2017) Probabilistic contact estimation and impact detection for state estimation of quadruped robots. *IEEE Robotics and Automation Letters* 2(2): 1023–1030.
- Carpentier J, Budhiraja R and Mansard N (2021) Proximal and sparse resolution of constrained dynamic equations. In: *Robotics: Science and Systems 2021*.
- Carpentier J, Saurel G, Buondonno G, Mirabel J, Lamiraux F, Stasse O and Mansard N (2019) The pinocchio c++ library: A fast and flexible implementation of rigid body dynamics algorithms and their analytical derivatives. In: *2019 IEEE/SICE International Symposium on System Integration (SII)*. IEEE, pp. 614–619.
- Cesa G, Lang L and Weiler M (2021) A program to build e (n)-equivariant steerable cnns. In: *International Conference on Learning Representations*.
- Chirikjian GS and Kyatkin AB (2000) *Engineering applications of noncommutative harmonic analysis: with emphasis on rotation and motion groups*. CRC press.
- Corbères T, Mastalli C, Merkt W, Havoutis I, Fallon M, Mansard N, Flayols T, Vijayakumar S and Tonneau S (2024) Perceptive locomotion through whole-body mpc and optimal region selection.
- Cornwell JF (1997) *Group theory in physics: An introduction*. Academic press.

- De Haan P, Cohen T and Brehmer J (2023) Euclidean, projective, conformal: Choosing a geometric algebra for equivariant transformers. *arXiv preprint arXiv:2311.04744* .
- Dresselhaus MS, Dresselhaus G and Jorio A (2007) *Group theory: application to the physics of condensed matter*. Springer Science & Business Media.
- Eves HW (1980) *Elementary matrix theory*. Courier Corporation.
- Featherstone R (2007) *Rigid Body Dynamics Algorithms*. Berlin, Heidelberg: Springer-Verlag.
- Feldman AG and Levin MF (2009) The equilibrium-point hypothesis—past, present and future. *Progress in motor control: A multidisciplinary perspective* : 699–726.
- Finzi M, Benton G and Wilson AG (2021) Residual pathway priors for soft equivariance constraints. *Advances in Neural Information Processing Systems* 34: 30037–30049.
- Golubitsky M, Stewart I and Schaeffer DG (2012) *Singularities and Groups in Bifurcation Theory: Volume II*, volume 69. Springer Science & Business Media.
- Griminger F, Meduri A, Khadiv M, Viereck J, Wüthrich M, Naveau M, Berenz V, Heim S, Widmaier F, Flayols T, Fiene J, Badri-Spröwitz A and Righetti L (2020) An open torque-controlled modular robot architecture for legged locomotion research. *IEEE Robotics and Automation Letters* 5(2): 3650–3657. DOI:10.1109/LRA.2020.2976639.
- Higgins I, Racanière S and Rezende D (2022) Symmetry-based representations for artificial and biological general intelligence. *Frontiers in Computational Neuroscience* : 28.
- Ijspeert AJ (2008) Central pattern generators for locomotion control in animals and robots: a review. *Neural networks* 21(4): 642–653.
- Jumper J, Evans R, Pritzel A, Green T, Figurnov M, Ronneberger O, Tunyasuvunakool K, Bates R, Žídek A, Potapenko A et al. (2021) Highly accurate protein structure prediction with alphafold. *Nature* 596(7873): 583–589.
- Katz B, Di Carlo J and Kim S (2019) Mini cheetah: A platform for pushing the limits of dynamic quadruped control. In: *2019 international conference on robotics and automation (ICRA)*. IEEE, pp. 6295–6301.
- Klein L, Krämer A and Noé F (2023) Equivariant flow matching. *arXiv preprint arXiv:2306.15030* .
- Knapp AW (1986) *Representation Theory of Semisimple Groups, An Overview Based on Examples (PMS-36)*. Princeton: Princeton University Press.
- Kobilarov M, Ta DN and Dellaert F (2015) Differential dynamic programming for optimal estimation. In: *IEEE International Conference on Robotics and Automation (ICRA)*.
- Lanczos C (2020) *The variational principles of mechanics*. University of Toronto press.
- Lee J, Hwangbo J, Wellhausen L, Koltun V and Hutter M (2020) Learning quadrupedal locomotion over challenging terrain. *Science robotics* 5(47): eabc5986.
- Li W and Todorov E (2004) Iterative linear quadratic regulator design for nonlinear biological movement systems. In: *First International Conference on Informatics in Control, Automation and Robotics*, volume 2. SciTePress.
- Lin TY, Zhang R, Yu J and Ghaffari M (2021) Legged robot state estimation using invariant kalman filtering and learned contact events. In: *5th Annual Conference on Robot Learning*.
- Mastalli C, Budhiraja R, Merkt W, Saurel G, Hammoud B, Naveau M, Carpentier J, Righetti L, Vijayakumar S and Mansard N (2020a) Crocodyl: An efficient and versatile framework for multi-contact optimal control. In: *IEEE International Conference on Robotics and Automation (ICRA)*.
- Mastalli C, Chhatoi SP, Corbères T, Tonneau S and Vijayakumar S (2023) Inverse-dynamics mpc via nullspace resolution. *IEEE Transactions on Robotics* 39.
- Mastalli C, Havoutis I, Focchi M, Caldwell DG and Semini C (2020b) Motion Planning for Quadrupedal Locomotion: Coupled Planning, Terrain Mapping, and Whole-Body Control. *IEEE Transactions on Robotics* 36.
- Mayne D (1966) A second-order gradient method for determining optimal trajectories of non-linear discrete-time systems. *International Journal of Control* 3.
- Mondal AK, Jain V, Siddiqi K and Ravanbakhsh S (2022) Eqr: Equivariant representations for data-efficient reinforcement learning. In: *International Conference on Machine Learning*. PMLR, pp. 15908–15926.
- Noé F, Tkatchenko A, Müller KR and Clementi C (2020) Machine learning for molecular simulation. *Annual review of physical chemistry* 71: 361–390.
- Ordoñez-Apraez D, Kostic V, Turrisi G, Novelli P, Mastalli C, Semini C and Pontil M (2023) Dynamics harmonic analysis of robotic systems: Application in data-driven koopman modelling. *arXiv preprint arXiv:2312.07457* .
- Ordonez-Apraez D, Martin M, Agudo A and Moreno-Noguer F (2023) On discrete symmetries of robotics systems: A group-theoretic and data-driven analysis. In: *Robotics Science and System (RSS)*.
- Orin DE, Goswami A and Lee SH (2013) Centroidal dynamics of a humanoid robot. *Autonomous robots* 35(2): 161–176.
- Ostrowski J and Burdick J (1996) Geometric perspectives on the mechanics and control of robotic locomotion. In: *Robotics Research*. Springer, pp. 536–547.
- Quigley RJ (1973) Pseudovectors and reflections. *American Journal of Physics* 41(3): 428–430.
- Rezaei-Shoshtari S, Zhao R, Panangaden P, Meger D and Precup D (2022) Continuous mdp homomorphisms and homomorphic policy gradient. *Advances in Neural Information Processing Systems* 35: 20189–20204.
- Schaal S, Peters J, Nakanishi J and Ijspeert A (2003) Control, planning, learning, and imitation with dynamic movement primitives. In: *Workshop on Bilateral Paradigms on Humans and Humanoids: IEEE International Conference on Intelligent Robots and Systems (IROS 2003)*. pp. 1–21.
- Scholz JP and Schöner G (1999) The uncontrolled manifold concept: identifying control variables for a functional task. *Experimental brain research* 126: 289–306.
- Selig JM (2005) *Geometric fundamentals of robotics*, volume 128. Springer.
- Solà J, Deray J and Atchuthan D (2021) A micro Lie theory for state estimation in robotics.
- Sutton RS and Barto AG (2018) *Reinforcement learning: An introduction*. MIT press.
- Tassa Y, Mansard N and Todorov E (2014) Control-limited differential dynamic programming. In: *IEEE International Conference on Robotics and Automation (ICRA)*. IEEE, pp. 1168–1175.

- Traversaro S, Brossette S, Escande A and Nori F (2016) Identification of fully physical consistent inertial parameters using optimization on manifolds. In: IEEE/RSJ International Conference on Intelligent Robots and Systems (IROS).
- Van der Pol E, Worrall D, van Hoof H, Oliehoek F and Welling M (2020) Mdp homomorphic networks: Group symmetries in reinforcement learning. Advances in Neural Information Processing Systems 33: 4199–4210.
- Wang D, Jia M, Zhu X, Walters R and Platt R (2022a) On-robot learning with equivariant models. arXiv preprint arXiv:2203.04923 .
- Wang D, Walters R and Platt R (2022b) So(2)-equivariant reinforcement learning. arXiv preprint arXiv:2203.04439 .
- Wang R, Walters R and Yu R (2022c) Approximately equivariant networks for imperfectly symmetric dynamics. arXiv preprint arXiv:2201.11969 .
- Weiler M, Forré P, Verlinde E and Welling M (2023) Equivariant and Coordinate Independent Convolutional Networks.
- Weissenbacher M, Sinha S, Garg A and Yoshinobu K (2022) Koopman q-learning: Offline reinforcement learning via symmetries of dynamics. In: International Conference on Machine Learning. PMLR, pp. 23645–23667.
- Wheeler JT (2014) General coordinate covariance of the euler lagrange equations. Classical Mechanics class notes.
- Wieber PB (2006) Holonomy and nonholonomy in the dynamics of articulated motion. In: Fast motions in biomechanics and robotics. Springer, pp. 411–425.
- Zinkevich M and Balch T (2001) Symmetry in markov decision processes and its implications for single agent and multi agent learning. In: In Proceedings of the 18th International Conference on Machine Learning. Citeseer.

Special Terms

- CMM** centroidal momentum matrix. 15
- CNN** convolutional neural network. 16
- CNN_{aug}** CNN trained with data augmentation. 16
- CoM** The center of mass refers to the centroidal point of a distribution of mass in space. This is often referred to as the barycenter or balance point . 8, 15
- DHA** The term Dynamics Harmonics Analysis, introduced in Ordoñez-Apaez et al. (2023), refers to the decomposition of the system’s dynamics into a superposition of lower-dimensional, independent dynamics. This concept is inspired from the goal of abstract harmonic analysis, namely, to decompose functions (in this case, the system’s set of differential equations of motion) into a superposition of simpler, symmetric functions (in this case the dynamics of each Normal Configuration Mode (NCM) of motion). This use of abstract harmonic analysis is also referred to the literature as a generalized Fourier transformation (Chirikjian and Kyatkin 2000).. 11, 12, 15, 18
- DoF** degrees of freedom. 6, 9–11, 14, 15
- eCNN** equivariant CNN. 16
- eMLP** equivariant multi layer perceptron. 15, 16
- EoM** equations of motion. 5, 7
- MDP** Markov decision process. 14
- MLP** multi layer perceptron. 15, 16
- MLP_{aug}** MLP with data augmentation. 15, 16
- NCM** The term Normal Configuration Mode (NCM) of motion, introduced in this work, denotes a unique mode of symmetry-constrained motion of a robot configuration. The qualifier ”Normal” underscores the orthogonality